

Reconstruction of optical properties of phantom and breast lesion *in vivo* from paraxial scanning data

Thomas Dierkes¹, Dirk Grosenick², K Thomas Moesta³, Michael Möller², Peter M Schlag³, Herbert Rinneberg² and Simon Arridge¹

¹ Department of Computer Science, University College London, Gower Street, London WC1E 6BT, UK

² Physikalisch-Technische Bundesanstalt, Abbestraße 2-12, 10587 Berlin, Germany

³ Department of Surgery and Surgical Oncology, Robert-Rössle-Hospital, Charité, Campus Buch, Lindenberger Weg 80, 13125 Berlin, Germany

E-mail: dirk.grosenick@ptb.de

Received 1 November 2004, in final form 7 April 2005

Published 18 May 2005

Online at stacks.iop.org/PMB/50/2519

Abstract

We report on the reconstruction of absorption and reduced scattering coefficients of breast tissue *in vivo* of a patient with mastopathic disease. Distributions of times of flight of photons through the compressed breast were recorded by paraxial scanning. From data measured at four different source–detector offsets optical properties were reconstructed within the linear Rytov approximation by a fast inverse Fourier space method. Low-pass filtering in Fourier space was employed to remove excessive noise from high spatial frequency components and to reduce the computational efforts by a factor of 3, typically. The mammograms displaying reconstructed absorption and reduced scattering coefficients were compared with projection mammograms either obtained by time-window analysis of experimental data or based on average absorption and reduced scattering coefficients which were derived from measured temporal point spread functions within a simple homogeneous model. All inhomogeneities which were visible in the projection mammograms and which could be associated with specific breast tissue compartments could be correlated with inhomogeneities in the reconstructed absorption coefficient. In particular, the mastopathic disease was detected in the reconstructed absorption mammogram. In order to assess reliability of optical properties reconstructed from data obtained by paraxial scanning, corresponding phantom experiments and reconstructions of phantom optical properties were carried out. Because of the limited angular range sampled by the *in vivo* and phantom measurements, considerable blurring of the absorption coefficient occurs along the compression direction, compromising longitudinal resolution.

1. Introduction

Near infrared light diffusing through thick biological tissue can be used to non-invasively probe its absorption and scattering properties. In particular, when broadband red to near infrared radiation is employed or light at several selected wavelengths within this spectral range is used, information can be gained on, e.g., tissue composition, its biochemical and metabolic state and on pathological processes leading to changes in absorption and scattering of tissue (Cerussi *et al* 2002). Diffuse optical tomography aims at reconstructing the absorption and reduced scattering coefficients of the diffusely scattering medium from measurements of transmitted or re-emitted light (Arridge 1999). Optical mammography is one of several applications of diffuse optical tomography that are currently being developed for biomedical research and for clinical use as well.

There is a large variety of experimental systems in use today to record optical mammograms, differing in their arrangement of sources and detectors as well as in the type of laser radiation employed. Most optical mammographs utilize sinusoidally amplitude-modulated laser light (frequency-domain systems, Franceschini *et al* 1997, Götz *et al* 1998, Dehghani *et al* 2003), but there are also systems, employing continuous (cw) laser radiation (cw-mammographs, Colak *et al* 1999) and even hybrid systems (Culver *et al* 2003), whereas time-domain mammographs (Grosenick *et al* 1999, Pifferi *et al* 2003, Yates *et al* 2005) use ultrashort laser pulses as input. The latter systems measure the temporal dispersion of the transmitted laser pulse (temporal point spread functions, TPSFs, distributions of times of flight of photons, DTOFs) at a resolution of typically tens to hundreds of picoseconds. Frequency-domain systems on the other hand measure phase shift and modulation amplitude at frequencies of typically 100 MHz, corresponding to a measurement of the complex intensity of the transmitted photon density wave.

To gain true tomographic information on absorption and reduced scattering coefficients of breast tissue, 3D arrangements of source and detector optical fibres around the freely suspended breast are used to record transmittance at various projection angles (Colak *et al* 1999, Dehghani *et al* 2003, Yates *et al* 2005). Tissue optical properties are reconstructed from such measurements in order to generate optical mammograms, which requires the solution of an ill-posed problem. Alternatively, the breast may be compressed between two parallel glass plates and data collected using stationary 2D arrangements of optical sources and detectors on both compression plates (Culver *et al* 2003), or by scanning one source fibre and one or several detector fibres synchronously across both compression plates (Franceschini *et al* 1997, Götz *et al* 1998, Grosenick *et al* 1999, Pifferi *et al* 2003). Because light is strongly attenuated when diffusing through several centimetres of tissue, the parallel plane transmission geometry offers considerable advantages with respect to signal strength. Furthermore, such instruments provide projection images corresponding to an x-ray radiograph, without the need to reconstruct the absorption and scattering properties of the tissue. Such projection mammograms can be compared with x-ray or MR-mammograms, e.g. for validation.

Scanning mammographs with parallel plane geometry generally sample a large number of source and detector positions and provide good lateral resolution for inhomogeneities close to the breast surface. Generally, however, only a small number of lateral source–detector offsets is used and therefore sampling of various projection angles is very restricted (paraxial scanning). By contrast in order to reconstruct three-dimensional images of the compressed breast, it is necessary to make multiple measurements for each source position. Culver *et al* (2003) reported on 3D optical tomography of a healthy volunteer's breast compressed between two glass plates using 45 source positions on the source plane and 576 detector positions on the opposite glass plate, reconstructing the absorption coefficient from the dc intensity of the

diffusely transmitted light, measured for each source–detector pair. Ideally, the data available are over a complete 2D manifold for each source position. If only measurements over a restricted range of projection angles are available, one may still attempt to reconstruct an image notwithstanding the extra degree of ill-posedness that is thereby introduced.

In general, the image reconstruction problem has to be considered as nonlinear which involves a parametrized model, such as finite elements, finite differences or finite volumes and adjusts these parameters in order to optimize an objective function combining a data fitting and regularization term (Arridge *et al* 1993, Schweiger *et al* 1993, 1995, Paulsen and Jiang 1995, Klose and Hielscher 1999). These methods, based on the diffusion equation or the radiative transfer equation use a variety of algorithms, including Newton, quasi-Newton and nonlinear conjugate gradients to minimize the objective function over the search space of model parameters. A simpler approach to reconstruction is to assume that the required image differs from a known background image by only a small amount. In this case it is possible to linearize the nonlinear approach and to represent the problem as involving the inversion of a linear integral equation (O’Leary *et al* 1995). This model can be constructed using Green’s functions for the diffusion equation, either in infinite space or in volumes of simple shape, or in the presence of boundaries of general shape by a numerical technique such as Monte Carlo, finite elements, finite differences or finite volumes (Walker *et al* 1997, Ripoll *et al* 2001).

Rather than solving the inverse problem in real space, one may carry out reconstructions of optical properties in Fourier space. This approach was followed by several authors previously. Li *et al* (1997, 2000) reconstructed absorption and diffusion coefficients of a narrow slice in an infinite turbid medium from frequency-domain data transformed into Fourier space, using an angular spectrum algorithm. In several publications, Markel and Schotland theoretically investigated the reconstruction of absorption and reduced scattering coefficients of an infinite slab of a turbid medium (Markel and Schotland 2001, 2002a), providing inversion formulae based on Fourier–Laplace transforms. These authors also considered reconstruction of limited data obtained by paraxial scanning (Markel and Schotland 2002b, 2002c).

In this paper, we apply the linearized approach to phantom data and *in vivo* optical mammograms, recorded with time-domain instrumentation and paraxial scanning. Therefore, the amount of data is very large and the inversion of the corresponding set of linear equations would be computationally expensive. We therefore follow an approach for data reduction that appears to give reasonable reconstructions with a much smaller computational effort. The main idea is to firstly take a Fourier transform in time to select only a small number of harmonic frequencies, and secondly to apply a spatial Fourier transformation and low-pass filter to the projections. The measured data are therefore inverted in Fourier domain, both in time and space prior to reconstruction of optical properties.

2. Theory

2.1. Linear perturbation theory and the Rytov approximation

In this section, we briefly summarize the equations governing the diffusion of photons within an inhomogeneous turbid medium. Within the diffusion approximation, the photon density $u(\vec{r}, \vec{r}_S, t)$ at time t and location \vec{r} in the medium, following injection of a short δ -like laser pulse $S(\vec{r}, t) = N_{\text{ph}}\delta_0(t)\delta_0(\vec{r} - \vec{r}_S)$ satisfies the parabolic differential equation

$$\frac{\partial}{\partial t}u(\vec{r}, \vec{r}_S, t) = \nabla_r(D(\vec{r})\nabla_r)u(\vec{r}, \vec{r}_S, t) - c\mu_a(\vec{r})u(\vec{r}, \vec{r}_S, t) + N_{\text{ph}}\delta_0(t)\delta_0(\vec{r} - \vec{r}_S). \quad (1)$$

Here $\mu_a(\vec{r})$ denotes the absorption coefficient, $D(\vec{r})$ the diffusion coefficient, $c = c_0/n$ is the speed of light in the turbid medium with index of refraction n , assumed to be constant, and N_{ph}

the number of photons contained in the light pulse. The diffusion coefficient is expressed as $D(\vec{r}) = c/\{3(\mu_a(\vec{r}) + \mu'_s(\vec{r}))\}$ and $\mu'_s(\vec{r})$ stands for the reduced scattering coefficient. Setting

$$D(\vec{r}) = D_0 + \delta D(\vec{r}), \quad \text{and} \quad \mu_a(\vec{r}) = \mu_{a0} + \delta\mu_a(\vec{r}) \quad (2)$$

the Fourier transform $\hat{u}(\vec{r}, \vec{r}_S, \omega)$

$$\hat{u}(\vec{r}, \vec{r}_S, \omega) = \int_{-\infty}^{+\infty} u(\vec{r}, \vec{r}_S, t) \exp(i\omega t) dt \quad (3)$$

satisfies the modified Helmholtz equation

$$\nabla_r^2 \hat{u}(\vec{r}, \vec{r}_S, \omega) - k_0^2 \hat{u}(\vec{r}, \vec{r}_S, \omega) = \frac{1}{D_0} \{c\delta\mu_a(\vec{r}) - \nabla_r(\delta D(\vec{r})\nabla_r)\hat{u}(\vec{r}, \vec{r}_S, \omega)\} - \frac{N_{\text{ph}}}{D_0} \delta_0(\vec{r} - \vec{r}_S), \quad (4)$$

with

$$k_0^2 = \frac{c\mu_{a0} - i\omega}{D_0}. \quad (5)$$

The photon density per unit interval of angular frequency $\hat{u}(\vec{r}, \vec{r}_S, \omega)$ corresponds to an incident intensity modulated light source proportional to $\exp(-i\omega t)\delta_0(\vec{r} - \vec{r}_S)$. Using the Green's function $G_0(\vec{r}, \vec{r}', \omega)$ which satisfies the following differential equation:

$$(\nabla_r^2 - k_0^2)G_0(\vec{r}, \vec{r}', \omega) = -\frac{1}{D_0}\delta_0(\vec{r} - \vec{r}'), \quad (6)$$

or equivalently, the solution $\hat{u}_0(\vec{r}, \vec{r}_S, \omega) = N_{\text{ph}}G_0(\vec{r}, \vec{r}_S, \omega)$ for the homogeneous medium ($\delta\mu_a(\vec{r}) = 0, \delta D(\vec{r}) = 0$), equation (4) can be formally integrated yielding

$$\begin{aligned} \hat{u}(\vec{r}, \vec{r}_S, \omega) &= \hat{u}_0(\vec{r}, \vec{r}_S, \omega) - \int_V G_0(\vec{r}, \vec{r}', \omega) [c\delta\mu_a(\vec{r}') - \nabla_{r'}(\delta D(\vec{r}')\nabla_{r'})]\hat{u}(\vec{r}', \vec{r}_S, \omega) d^3r' \\ &+ D_0 \oint_{\Omega} [G_0(\vec{r}, \vec{r}', \omega)\vec{n}\nabla_{r'}\hat{u}(\vec{r}', \vec{r}_S, \omega) - \hat{u}(\vec{r}', \vec{r}_S, \omega)\vec{n}\nabla_{r'}G_0(\vec{r}, \vec{r}', \omega)] d^2r', \end{aligned} \quad (7)$$

where \vec{n} is the outward pointing surface normal. The solutions $\hat{u}(\vec{r}, \vec{r}_S, \omega)$ and $\hat{u}_0(\vec{r}, \vec{r}_S, \omega)$, $G_0(\vec{r}, \vec{r}_S, \omega)$ of equations (6) and (7), respectively, must obey boundary conditions. Two situations will be considered in the following, i.e. the infinite medium and the infinite slab of thickness d . In the first case, the surface integral in equation (7) vanishes when taken over a closed surface Ω at infinity because the spectral photon densities $\hat{u}(\vec{r}, \vec{r}_S, \omega)$, $\hat{u}_0(\vec{r}, \vec{r}_S, \omega)$ and $G_0(\vec{r}, \vec{r}_S, \omega)$ vanish at infinity. For the infinite slab we assume the spectral photon densities to obey the boundary conditions

$$v(\vec{r}, \vec{r}_S, \omega) = -z_e \vec{n} \nabla_r v(\vec{r}, \vec{r}_S, \omega)|_{\vec{r} \in \Omega}, \quad (8)$$

where z_e is the extrapolation distance, $\vec{r}_S = (x_S, y_S, z_S = 1/\mu'_{s0})$ is the position of the photon source inside the medium and $v(\vec{r}, \vec{r}_S, \omega)$ stands for any of the quantities $\hat{u}(\vec{r}, \vec{r}_S, \omega)$, $\hat{u}_0(\vec{r}, \vec{r}_S, \omega)$ and $G_0(\vec{r}, \vec{r}_S, \omega)$. Under these assumptions the surface integral in equation (7) vanishes for the infinite slab as well. Then, equation (7) may be rewritten as

$$\begin{aligned} \hat{u}(\vec{r}, \vec{r}_S, \omega) &= \hat{u}_0(\vec{r}, \vec{r}_S, \omega) - \int_V G_0(\vec{r}, \vec{r}', \omega) c\delta\mu_a(\vec{r}')\hat{u}(\vec{r}', \vec{r}_S, \omega) d^3r' \\ &- \int_V (\nabla_{r'}G_0(\vec{r}, \vec{r}', \omega))\delta D(\vec{r}')(\nabla_{r'}\hat{u}(\vec{r}', \vec{r}_S, \omega)) d^3r' \\ &+ \oint_{\Omega} G_0(\vec{r}, \vec{r}', \omega)\delta D_0(\vec{r}')\vec{n}\nabla_{r'}\hat{u}(\vec{r}', \vec{r}_S, \omega) d^2r'. \end{aligned} \quad (9)$$

Again, the surface integral in equation (9) is zero for the infinite medium. For the infinite slab, however, we assume $\delta D(\vec{r})$ to be zero on the surface Ω , since we are interested in inhomogeneities located inside the slab. In the following we solve equation (9) by setting

$$\hat{u}(\vec{r}, \vec{r}_S, \omega) = \hat{u}_0(\vec{r}, \vec{r}_S, \omega) \exp\{w_R(\vec{r}, \vec{r}_S, \omega)\}. \quad (10)$$

The Rytov *ansatz* (equation (10)) accounts for changes from the homogeneous solution $\hat{u}_0(\vec{r}, \vec{r}_S, \omega)$ by introducing a complex phase $w_R(\vec{r}, \vec{r}_S, \omega)$ whereas the well-known Born *ansatz* considers a scattered amplitude which adds to the homogeneous solution (Kak and Slaney 1988, O'Leary 1996). We derive $w_R(\vec{r}, \vec{r}_S, \omega)$ within linear approximation (the Rytov approximation), using as Green's functions

$$G_0^{\text{inf}}(\vec{r}, \vec{r}', \omega) = \frac{1}{4\pi D_0 |\vec{r} - \vec{r}'|} \exp(-k_0 |\vec{r} - \vec{r}'|) \quad (11)$$

$$G_0^{\text{slab}}(\vec{r}, \vec{r}', \omega) = \sum_{n=-\infty}^{\infty} \{G_0^{\text{inf}}(\vec{r}, \vec{r}'_{+n}, \omega) - G_0^{\text{inf}}(\vec{r}, \vec{r}'_{-n}, \omega)\}$$

for the infinite medium and the infinite slab, respectively, where $\vec{r}'_{+n} = (x', y', 2nd + 4nz_e + z')$ and $\vec{r}'_{-n} = (x', y', 2nd + (4n - 2)z_e - z')$. To this end the exponential $\exp\{w_R(\vec{r}, \vec{r}_S, \omega)\}$ is expanded to first order and $\hat{u}(\vec{r}, \vec{r}_S, \omega)$ is replaced by $\hat{u}_0(\vec{r}, \vec{r}_S, \omega)$ on the right-hand side of equation (9), i.e. by the spectral photon density of the homogeneous infinite medium or infinite slab, depending on the model used. In this way one obtains at the detector position $\vec{r} = \vec{r}_D$

$$\hat{u}_0(\vec{r}_D, \vec{r}_S, \omega) w_R(\vec{r}_D, \vec{r}_S, \omega) = - \int_V G_0(\vec{r}_D, \vec{r}', \omega) c \delta \mu_a(\vec{r}') \hat{u}_0(\vec{r}', \vec{r}_S, \omega) d^3 r' \\ - \int_V (\nabla_{r'} G_0(\vec{r}_D, \vec{r}', \omega)) \delta D(\vec{r}') (\nabla_{r'} \hat{u}_0(\vec{r}', \vec{r}_S, \omega)) d^3 r'. \quad (12)$$

Setting

$$K_a(\vec{r}_D, \vec{r}', \vec{r}_S, \omega) = -c G_0(\vec{r}_D, \vec{r}', \omega) \hat{u}_0(\vec{r}', \vec{r}_S, \omega) / \hat{u}_0(\vec{r}_D, \vec{r}_S, \omega) \quad (13)$$

$$K_D(\vec{r}_D, \vec{r}', \vec{r}_S, \omega) = -(\nabla_{r'} G_0(\vec{r}_D, \vec{r}', \omega)) (\nabla_{r'} \hat{u}_0(\vec{r}', \vec{r}_S, \omega)) / \hat{u}_0(\vec{r}_D, \vec{r}_S, \omega)$$

we express $w_R(\vec{r}_D, \vec{r}_S, \omega)$ as

$$w_R(\vec{r}_D, \vec{r}_S, \omega) = \int_V \{K_a(\vec{r}_D, \vec{r}', \vec{r}_S, \omega) \delta \mu_a(\vec{r}') + K_D(\vec{r}_D, \vec{r}', \vec{r}_S, \omega) \delta D(\vec{r}')\} d^3 r' \quad (14)$$

Equation (14) allows us to reconstruct $\delta \mu_a(\vec{r})$ and $\delta D(\vec{r})$ from experimental data by setting

$$w_R(\vec{r}_D, \vec{r}_S, \omega) = \ln\{\hat{N}(\vec{r}_D, \vec{r}_S, \omega) / \hat{N}_0(\vec{r}_D, \vec{r}_S, \omega)\}, \quad (15)$$

i.e. by replacing the ratio $\hat{u}(\vec{r}_D, \vec{r}_S, \omega) / \hat{u}_0(\vec{r}_D, \vec{r}_S, \omega)$ (see equation (10)) by the ratio of the Fourier components of measured DTOFs (TPSFs) $N(\vec{r}_D, \vec{r}_S, t)$ and $N_0(\vec{r}_D, \vec{r}_S, t)$, where $N_0(\vec{r}_D, \vec{r}_S, t)$ refers to the homogeneous medium ($\delta \mu_a(\vec{r}) = 0$, $\delta D(\vec{r}) = 0$).

2.2. Inverse Fourier space method and computational details

2.2.1. Paraxial scanning.

In scanning optical mammography, the breast is compressed between two parallel glass plates and TPSFs $N(\vec{r}_D, \vec{r}_S, t)$ are sampled at a limited number of source (\vec{r}_S) and detector (\vec{r}_D) positions by moving the source and detector optical fibres in tandem across the source plane ($z = 0$) and detector plane ($z = d$), respectively, i.e. keeping the lateral source–detector offset $\delta \vec{\rho} = \vec{\rho}_D - \vec{\rho}_S = (x_D - x_S, y_D - y_S)$ constant. Generally, scans are recorded at a few selected offsets $\delta \vec{\rho}_r$ ($r = 1, \dots, N_{\text{off}}$) only (paraxial scanning). The source fibre moves by increments Δx_{step} and Δy_{step} , along the x - and y -directions, respectively,

covering an area $L_{x,r} \times L_{y,r}$, where $L_{x,r} = N_{\text{step},r} \Delta x_{\text{step}}$ and $L_{y,r} = M_{\text{step},r} \Delta y_{\text{step}}$, with x -scans taken parallel to the chest wall. Generally, the number of steps along the x -axis ($N_{\text{step},r} - 1$) and y -axis ($M_{\text{step},r} - 1$) as well as the start position of the source fibre, $\vec{\rho}_{S0} = (x_{S,\text{min},r}, y_{S,\text{min},r})$ may depend on the size of the particular offset ($\delta\vec{\rho}_r$) chosen. In this way the source positions $\vec{r}_{Sj,k} = \vec{\rho}_{Sj,k} + z_S \vec{e}_z$ and associated detector positions $\vec{r}_{Dj,k,r} = \vec{\rho}_{Sj,k} + \delta\vec{\rho}_r + d\vec{e}_z$ are sampled, with $\vec{\rho}_{Sj,k} = (x_{S,\text{min},r} + j\Delta x_{\text{step}}, y_{S,\text{min},r} + k\Delta y_{\text{step}})$, $j = 0, 1, \dots, (N_{\text{step},r} - 1)$, and $k = 0, 1, \dots, (M_{\text{step},r} - 1)$.

2.2.2. Inverse Fourier space method. Following Markel and Schotland (2001, 2002a) we first carry out a 2D Fourier transformation of equation (14) over the source positions $\vec{\rho}_S$ for each lateral source–detector offset $\delta\vec{\rho}$ separately, rather than reconstructing $\delta\mu_a(\vec{r})$ and $\delta D(\vec{r})$ from equation (14) directly. Unlike these authors, who derived analytical expressions for the 2D Fourier transforms, in this paper discrete Fourier transforms of the kernels $K_a(\vec{\rho}_{Sj,k} + \delta\vec{\rho}_r, z_D, \vec{r}'_\ell, \vec{\rho}_{Sj,k}, z_S, \omega)$, $K_D(\vec{\rho}_{Sj,k} + \delta\vec{\rho}_r, z_D, \vec{r}'_\ell, \vec{\rho}_{Sj,k}, z_S, \omega)$, (cf equation (13)) and of the data $w_R(\vec{\rho}_{Sj,k} + \delta\vec{\rho}_r, z_D, \vec{\rho}_{Sj,k}, z_S, \omega)$, (cf equations (14), (15)) are calculated numerically. To this end we discretize equations (13)–(15) by dividing the rectangular volume of the object (phantom, compressed breast), the optical properties of which are to be reconstructed, into N_{vox} voxels of volume $\Delta V = h_x \times h_y \times h_z$, denote the position vector of the ℓ th voxel by \vec{r}_ℓ and set $\delta\mu_a^{\text{nm}} = \delta\mu_a^{\text{nm}}(\vec{r}_\ell) = \delta\mu_a(\vec{r}_\ell)/\mu_{a0}$, $\delta D_\ell^{\text{nm}} = \delta D^{\text{nm}}(\vec{r}_\ell) = \delta D(\vec{r}_\ell)/D_0$. Furthermore, we use as abbreviations

$$\begin{aligned} K_{aj,k,r,\ell}(\omega) &= \mu_{a0} K_a(\vec{\rho}_{Sj,k} + \delta\vec{\rho}_r, z_D, \vec{r}'_\ell, \vec{\rho}_{Sj,k}, z_S, \omega) \Delta V \\ K_{Dj,k,r,\ell}(\omega) &= D_0 K_D(\vec{\rho}_{Sj,k} + \delta\vec{\rho}_r, z_D, \vec{r}'_\ell, \vec{\rho}_{Sj,k}, z_S, \omega) \Delta V \\ w_{Rj,k,r}(\omega) &= w_R(\vec{\rho}_{Sj,k} + \delta\vec{\rho}_r, z_D, \vec{\rho}_{Sj,k}, z_S, \omega) \end{aligned} \quad (16)$$

to calculate the 2D discrete Fourier transforms

$$\begin{aligned} \tilde{K}_{am,n,r,\ell}(\omega) &= \sum_{j,k} K_{aj,k,r,\ell}(\omega) e^{-2\pi i(jm/N_{\text{step},r} + kn/M_{\text{step},r})} \\ \tilde{K}_{Dm,n,r,\ell}(\omega) &= \sum_{j,k} K_{Dj,k,r,\ell}(\omega) e^{-2\pi i(jm/N_{\text{step},r} + kn/M_{\text{step},r})} \\ \tilde{w}_{Rm,n,r}(\omega) &= \sum_{j,k} w_{Rj,k,r}(\omega) e^{-2\pi i(jm/N_{\text{step},r} + kn/M_{\text{step},r})}, \\ j, m &= 0, 1, \dots, (N_{\text{step},r} - 1), \quad k, n = 0, 1, \dots, (M_{\text{step},r} - 1). \end{aligned} \quad (17)$$

It follows from equation (11) that for fixed source–detector offset $\delta\vec{\rho}_r$, the denominator

$$\begin{aligned} \hat{u}_0(\vec{\rho}_{Sj,k} + \delta\vec{\rho}_r, z_D, \vec{\rho}_{Sj,k}, z_S, \omega) &= N_{\text{ph}} G_0(\vec{\rho}_{Sj,k} + \delta\vec{\rho}_r, z_D, \vec{\rho}_{Sj,k}, z_S, \omega) \\ &= N_{\text{ph}} G_0(\delta\vec{\rho}_r, z_D - z_S, \vec{\rho}_S = \vec{0}, \omega) \end{aligned} \quad (18)$$

appearing in equations (13), (16) and (17) no longer depends on the source position $\vec{\rho}_{Sj,k}$ and hence may be taken out of the sum for each source–detector offset $\delta\vec{\rho}_r$ separately. The 2D discrete Fourier transform of the kernels K_a and K_D are then used to obtain the discretized equivalent of equation (14)

$$\tilde{w}_{Rm,n,r}(\omega) = \sum_{\ell=1}^{N_{\text{vox}}} \{ \tilde{K}_{am,n,r,\ell}(\omega) \delta\mu_a^{\text{nm}} + \tilde{K}_{Dm,n,r,\ell}(\omega) \delta D_\ell^{\text{nm}} \}. \quad (19)$$

In order to reconstruct $\delta\mu_a^{\text{nm}}(\vec{r}_\ell)$ and $\delta D^{\text{nm}}(\vec{r}_\ell)$ from experimental data using equation (19), we calculate $\tilde{w}_{Rm,n,r}(\omega)$ from equation (17) using

$$w_{Rj,k,r}(\omega) = \ln\{ \hat{N}(\vec{\rho}_{Sj,k} + \delta\vec{\rho}_r, z_D, \vec{\rho}_{Sj,k}, z_S, \omega) / \hat{N}_0(\vec{\rho}_{Sj,k} + \delta\vec{\rho}_r, z_D, \vec{\rho}_{Sj,k}, z_S, \omega) \}, \quad (20)$$

in analogy to the reconstruction of $\delta\mu_a(\vec{r})$ and $\delta D(\vec{r})$ when carried out in real space using equation (14). However, compared to real space, Fourier space allows for easy (low-pass) filtering of the data taking only low spatial frequencies into account. For simplicity, we allow in the following for the same (odd) number $N_{\ell p} \times M_{\ell p}$ of low-pass filtered spatial frequencies for each offset $\delta\vec{\rho}_r$, independent of r . In this case m takes on the values $m = 0, 1, \dots, (N_{\ell p} - 1)/2$ and $m = N_{\text{step},r} - (N_{\ell p} - 1)/2, \dots, N_{\text{step},r} - 1$ in equation (19) and likewise $n = 0, 1, \dots, (M_{\ell p} - 1)/2$ and $n = M_{\text{step}} - (M_{\ell p} - 1)/2, \dots, M_{\text{step}} - 1$. In this way contrast to noise ratio can be improved considerably without seriously degrading spatial resolution, because of the limited resolution of diffuse optical tomography. Furthermore, restricting ourselves to a few spatial frequencies considerably reduces the number of linear equations in equation (19). In order to guarantee the solution to be real valued, equation (19) may be separated into real and imaginary parts, yielding

$$\begin{aligned} \text{Re } \tilde{w}_{Rm,n,r}(\omega) &= \sum_{\ell=1}^{N_{\text{vox}}} \{ \text{Re } \tilde{K}_{am,n,r,\ell}(\omega) \delta\mu_{a\ell}^{\text{nr}} + \text{Re } \tilde{K}_{Dm,n,r,\ell}(\omega) \delta D_{\ell}^{\text{nr}} \} \\ \text{Im } \tilde{w}_{Rm,n,r}(\omega) &= \sum_{\ell=1}^{N_{\text{vox}}} \{ \text{Im } \tilde{K}_{am,n,r,\ell}(\omega) \delta\mu_{a\ell}^{\text{nr}} + \text{Im } \tilde{K}_{Dm,n,r,\ell}(\omega) \delta D_{\ell}^{\text{nr}} \} \end{aligned} \quad (21)$$

We may write equation (21) in matrix form

$$g(\omega) = Kf, \quad (22)$$

where

$$\begin{aligned} g(\omega) &= (g_1(\omega), \dots, g_{2N_{\text{meas}}}(\omega))^T \\ &= (\text{Re } \tilde{w}_{R0,0,r=1}, \text{Im } \tilde{w}_{R0,0,r=1}, \dots, \text{Re } \tilde{w}_{RN_{\ell p},0,r=1}, \text{Im } \tilde{w}_{RN_{\ell p},0,r=1}, \dots, \text{Im } \tilde{w}_{RN_{\ell p},M_{\ell p},r=1}, \\ &\quad \text{Re } \tilde{w}_{R0,0,r=2}, \text{Im } \tilde{w}_{R0,0,r=2}, \dots, \text{Re } \tilde{w}_{RN_{\ell p},M_{\ell p},N_{\text{off}}}, \text{Im } \tilde{w}_{RN_{\ell p},M_{\ell p},N_{\text{off}}})^T \end{aligned} \quad (23)$$

$$f = (f_1, \dots, f_{2N_{\text{vox}}})^T = (\delta\mu_{a1}^{\text{nr}}, \dots, \delta\mu_{aN_{\text{vox}}}^{\text{nr}}, \delta D_1^{\text{nr}}, \dots, \delta D_{N_{\text{vox}}}^{\text{nr}})^T \quad \text{and}$$

$$K = \begin{pmatrix} \text{Re } \tilde{K}_{a0,0,r=1,\ell=1}, \dots, \text{Re } \tilde{K}_{a0,0,r=1,N_{\text{vox}}}, & \text{Re } \tilde{K}_{D0,0,r=1,\ell=1}, \dots, \text{Re } \tilde{K}_{D0,0,r=1,N_{\text{vox}}} \\ \text{Im } \tilde{K}_{a0,0,r=1,\ell=1}, \dots, \text{Im } \tilde{K}_{a0,0,r=1,N_{\text{vox}}}, & \text{Im } \tilde{K}_{D0,0,r=1,\ell=1}, \dots, \text{Im } \tilde{K}_{D0,0,r=1,N_{\text{vox}}} \\ \vdots & \\ \text{Re } \tilde{K}_{aN_{\ell p},M_{\ell p},N_{\text{off}},\ell=1}, \dots, \text{Re } \tilde{K}_{aN_{\ell p},M_{\ell p},N_{\text{off}},N_{\text{vox}}}, & \text{Re } \tilde{K}_{DN_{\ell p},M_{\ell p},N_{\text{off}},\ell=1}, \dots, \text{Re } \tilde{K}_{DN_{\ell p},M_{\ell p},N_{\text{off}},N_{\text{vox}}} \\ \text{Im } \tilde{K}_{aN_{\ell p},M_{\ell p},N_{\text{off}},\ell=1}, \dots, \text{Im } \tilde{K}_{aN_{\ell p},M_{\ell p},N_{\text{off}},N_{\text{vox}}}, & \text{Im } \tilde{K}_{DN_{\ell p},M_{\ell p},N_{\text{off}},\ell=1}, \dots, \text{Im } \tilde{K}_{DN_{\ell p},M_{\ell p},N_{\text{off}},N_{\text{vox}}} \end{pmatrix}, \quad (24)$$

is the rectangular matrix of size $2N_{\text{meas}} \times 2N_{\text{vox}}$ corresponding to equation (22), with $N_{\text{meas}} = N_{\text{off}} \times N_{\ell p} \times M_{\ell p}$ and $(\dots)^T$ denoting the transpose. For simplicity, we have taken just one frequency ω into account, although additional (higher) frequencies may ease the ill-posedness of equation (22) and possibly improve (longitudinal) spatial resolution of the reconstructed optical properties (Markel and Schotland 2002b, 2004). Equation (22) may only be inverted stably by applying a regularization scheme, e.g. the Tikhonov–Phillips scheme, yielding

$$\alpha f + K^T K f = K^T g \quad \alpha > 0. \quad (25)$$

Equation (25) is solved for f using the Cholesky method. Furthermore, it follows from equation (20) that $w_{Rj,k,r}(\omega)$ requires a reference experiment on a homogeneous medium with optical properties μ_{a0} , D_0 to be carried out. Although such a procedure is feasible in the case of phantom experiments, it is not possible for *in vivo* measurements. In the latter case we

estimate $\hat{N}_0(\vec{\rho}_{Sj,k} + \delta\vec{\rho}_r, z_D, \vec{\rho}_{Sj,k}, z_S, \omega)$ as mean of the data $\hat{N}(\vec{\rho}_{Sj,k} + \delta\vec{\rho}_r, z_D, \vec{\rho}_{Sj,k}, z_S, \omega)$, i.e.

$$\hat{N}_0^{\text{ave}}(\delta\vec{\rho}_r, z_D - z_S, \vec{\rho}_S = \vec{0}, \omega) = \{N_{\text{step},r} \times M_{\text{step},r}\}^{-1} \times \sum_{j=0}^{N_{\text{step},r}-1} \sum_{k=0}^{M_{\text{step},r}-1} \hat{N}(\vec{\rho}_{Sj,k} + \delta\vec{\rho}_r, z_D, \vec{\rho}_{Sj,k}, z_S, \omega) \quad (26)$$

to obtain

$$w_{Rj,k,r}^{\text{ave}}(\omega) = \ln \left\{ \hat{N}(\vec{\rho}_{Sj,k} + \delta\vec{\rho}_r, z_D, \vec{\rho}_{Sj,k}, z_S, \omega) / \hat{N}_0^{\text{ave}}(\delta\vec{\rho}_r, z_D - z_S, \vec{\rho}_S = \vec{0}, \omega) \right\}. \quad (27)$$

This estimate reflects the shift invariance of the Green's function $G_0(\vec{r}_D, \vec{r}_S, \omega)$ of the infinite space or infinite slab as discussed in equation (18) and is therefore justified. Besides $w_{Rj,k,r}(\omega)$, the quantity $w_{Rj,k,r}^{\text{ave}}(\omega)$ will be used to solve equation (25) for $\delta\mu_a^{\text{nm}}(\vec{r}_\ell)$ and $\delta D^{\text{nm}}(\vec{r}_\ell)$.

2.2.3. Comparison of various input data for reconstruction of optical properties. It is instructive to compare raw experimental data $w_{Rj,k,r}(\omega)$ or $w_{Rj,k,r}^{\text{ave}}(\omega)$ with experimental data $w_{Rj,k,r}^{\text{lpf}}(\omega)$ or $w_{Rj,k,r}^{\text{ave,lpf}}(\omega)$, low-pass filtered in Fourier space and transformed into real space by inverse Fourier transformation. Such a comparison illustrates the suppression of noise associated with high spatial frequencies (see section 3.2). Low-pass filtered data $w_{Rj,k,r}^{\text{lpf}}(\omega)$ were calculated according to the following equation:

$$w_{Rj,k,r}^{\text{lpf}}(\omega) = \{N_{\text{step},r} \times M_{\text{step},r}\}^{-1} \sum_{m,n} \tilde{w}_{Rm,n,r}(\omega) e^{+2\pi i(jm/N_{\text{step},r} + kn/M_{\text{step},r})} \quad (28)$$

with $j = 0, 1, \dots, (N_{\text{step},r} - 1)$, $k = 0, 1, \dots, (M_{\text{step},r} - 1)$, taking only the $N_{\text{lp}} \times M_{\text{lp}}$ 'lowest' spatial frequencies (see above) into account. Low-pass filtered data $w_{Rj,k,r}^{\text{ave,lpf}}(\omega)$ were obtained analogously. Furthermore, experimental phantom data may be compared with simulated data obtained from the same (linear) forward models that are used in the reconstruction of optical properties, revealing limitations of both forward models employed. For this purpose the known geometry and background optical properties of the phantom, the position and size of inhomogeneities and their optical properties were used in the calculations. Simulated data were calculated from equation (14) in discretized form, i.e.

$$w_{Rj,k,r}^{\text{sim}}(\omega) = \Delta V \sum_{\ell=1}^{N_{\text{vox}}} \{K_a(\vec{\rho}_{Sj,k} + \delta\vec{\rho}_r, z_D, \vec{r}'_\ell, \vec{\rho}_{Sj,k}, z_S, \omega) \delta\mu_a(\vec{r}'_\ell) + K_D(\vec{\rho}_{Sj,k} + \delta\vec{\rho}_r, z_D, \vec{r}'_\ell, \vec{\rho}_{Sj,k}, z_S, \omega) \delta D(\vec{r}'_\ell)\}. \quad (29)$$

3. Recording and pre-processing of phantom data

3.1. Experimental set-up and recording of phantom data

We used a standard experimental set-up for measuring time-resolved transmittance through a liquid, diffusely scattering phantom consisting of a rectangular cuvette with inner dimensions of 26 cm (width) \times 26 cm (height) \times 6 cm (thickness) made from 6 mm thick glass plates, filled with dilute milk and containing two solid spherical inhomogeneities. Laser pulses (pulse width 2 ps) were generated by a mode-locked Ti:sapphire laser at a repetition rate of 76 MHz. The laser output beam was attenuated to typically 150 mW and coupled into an optical fibre (diameter: 600 μm , NA: 0.38) used for illumination. The laser light emerging from the transmitting fibre was focused onto the interface (source plane) between the front glass face of the cuvette and the scattering liquid. At the opposite (rear) glass face diffusely

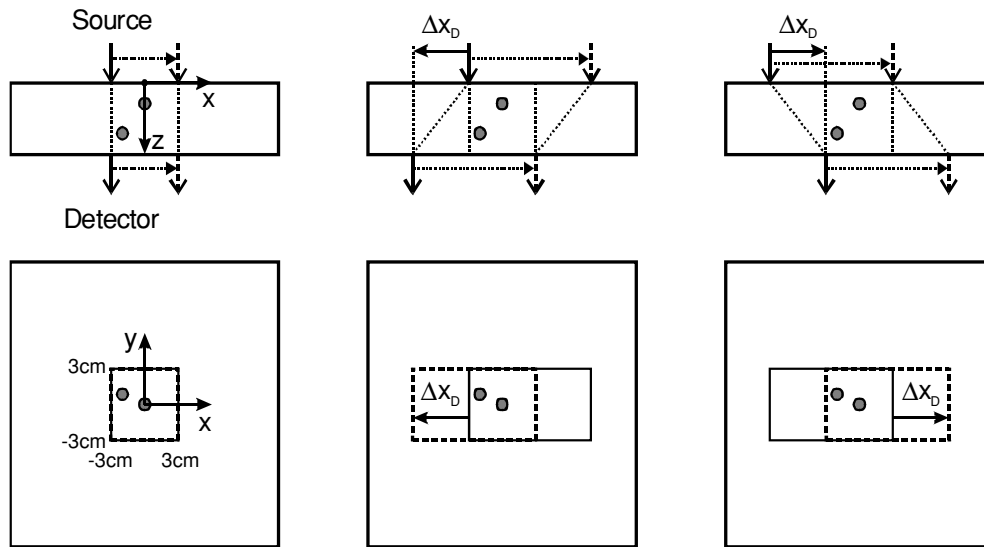


Figure 1. Phantom geometry and source–detector arrangement, with filled circles representing spherical inhomogeneities; top row: top view of phantom illustrating source and detector scan range along the x direction for three different offsets $\Delta x_D = x_D - x_S$ between source (x_S) and detector (x_D) fibre, i.e. for $\Delta x_D = 0$ (left), $\Delta x_D < 0$ (middle) and $\Delta x_D > 0$ (right); bottom row: view from detector side, the solid and dashed rectangles indicate the scan range of the source and detector fibre, respectively.

transmitted light pulses were collected by an optical fibre of the same kind and detected by a cooled microchannel-plate photomultiplier tube (MCP-PMT, Hamamatsu R2809U-11). Distributions of times of flight of photons were recorded using a time-correlated single photon counting system (SPC 300, Becker&Hickl GmbH, Germany). Taking the centre of the source plane as origin of the (right-handed) co-ordinate system x, y, z and its z -axis along the (horizontal) direction of illumination, the two 1 cm diameter spherical inhomogeneities suspended from nylon strings were positioned at $x_1^{\text{sph}} = -2$ cm, $y_1^{\text{sph}} = 0.85$ cm, $z_1^{\text{sph}} = 4.5$ cm and $x_2^{\text{sph}} = 0$ cm, $y_2^{\text{sph}} = 0$ cm, $z_2^{\text{sph}} = 1.5$ cm, respectively (figure 1). Paraxial scanning was carried out along the horizontal x -axis at various heights y_S (-3 cm $\leq y_S \leq 3$ cm) at increments $\Delta x_{\text{step}} = \Delta y_{\text{step}} = 0.25$ cm and for 11 offsets $\delta \vec{\rho} = (\Delta x_D, 0)$, with $\Delta x_D = x_D - x_S = 0, \pm 1$ cm, ± 2 cm, $\dots \pm 5$ cm. For $\Delta x_D \neq 0$, scan ranges of the source and detector optical fibres were augmented to the left and right as indicated in figure 1, e.g. $(-3$ cm $- \Delta x_D) \leq x_S \leq 3$ cm for $\Delta x_D > 0$. At fixed offset $\delta \vec{\rho} = (\Delta x_D, 0)$ we collected data at $N_{\text{step}} \times M_{\text{step}}$ scan positions with $N_{\text{step}} = 25, 29, \dots 45$ for $\Delta x_D = 0, \pm 1$ cm, $\dots \pm 5$ cm and $M_{\text{step}} = 25$. A total of 9875 scan positions were sampled including all offsets. At each scan position between 50 000 and 150 000 photons were collected within 3 s, depending on the offset $\delta \vec{\rho}$ chosen. All measurements on phantoms were carried out at $\lambda = 780$ nm. A small fraction of the laser output beam was coupled into a second optical fibre guiding the laser pulse directly to the photocathode of the MCP-PMT for providing a reference pulse.

As scattering medium we used a mixture of water and homogenized whole milk to which several millilitres of strongly diluted black indian ink was added. The (background) reduced scattering and absorption coefficients were determined to be $\mu'_{s0} = (13.0 \pm 1.3)$ cm $^{-1}$ and $\mu_{a0} = (0.039 \pm 0.003)$ cm $^{-1}$, respectively ($D_0 = (5.8 \pm 0.6) 10^8$ cm 2 s $^{-1}$, assuming $n_{\text{liquid}} = 1.33$), deduced from time-resolved transmittance through the cuvette with the solid inhomogeneities removed. To this end the solution of the diffusion equation for a homogeneous infinite slab

using extrapolated boundary conditions, convolved with the instrumental response function was fitted to the measured distributions of times of flight of photons. The spheres were made from a block of solid polymer ($n_{\text{solid}} = 1.55$) of dimensions 10 cm (width) \times 10 cm (height) \times 3 cm (thickness), that had been checked for homogeneity by recording time-resolved transmittance at a large number of scan positions, using the experimental set-up described above. From measured distributions of times of flight of photons the reduced scattering and absorption coefficient of the bulk polymer material were determined to be $\mu'_{\text{s,sph}} = (12.1 \pm 0.6) \text{ cm}^{-1}$ and $\mu_{\text{a,sph}} = (0.084 \pm 0.004) \text{ cm}^{-1}$, ($D_{\text{sph}} = (5.3 \pm 0.3) 10^8 \text{ cm}^2 \text{ s}^{-1}$) using the appropriate analytical solution of the diffusion equation. In addition, the optical properties of each sphere suspended in the liquid phantom were determined from time-resolved transmittance measured with an on-axis arrangement of the source fibre, the spherical inhomogeneity and the detector fibre using the model of diffraction of diffuse photon density waves in the analysis. The absorption coefficient and reduced scattering coefficient of the spheres determined in this way agreed within 10% and 5%, respectively, with the corresponding coefficients of the bulk polymer material. The background optical properties $\mu'_{\text{s}0}$, $\mu_{\text{a}0}$ of the phantom and the optical properties $\mu'_{\text{s,sph}}$, $\mu_{\text{a,sph}}$ of the spheres are typical for the absorption and scattering properties of breast tissue and breast tumours in the NIR range (Grosenick *et al* 2005).

Since the theoretical model (see section 2.1) used for reconstruction of optical properties does not take changes in the index of refraction into account and hence omits Fresnel reflections occurring at the solid/liquid interface of the spherical inhomogeneities in our phantom, we estimated the error made in deriving the transport scattering coefficient when the difference between the indices of refraction of the liquid and the solid material is neglected. For this purpose we simulated the time-resolved photon flux density in transmission geometry at zero source–detector offset for the phantom, containing one sphere only ($x_2^{\text{sph}} = 0 \text{ cm}$, $y_2^{\text{sph}} = 0 \text{ cm}$, $z_2^{\text{sph}} = 1.5 \text{ cm}$, $r = 0.5 \text{ cm}$). Simulations were carried out using the diffraction of photon density waves setting the reduced scattering coefficient of the inhomogeneity equal to that of the surrounding liquid ($\mu'_{\text{s}0} = 13.0 \text{ cm}^{-1}$), but taking into account the different indices of refraction. Subsequently the simulated time-resolved flux densities were analysed for the absorption and reduced scattering coefficients of the spherical inhomogeneity using the same model (diffraction of photon density waves) but taking both indices of refraction to be equal. The absorption coefficient of the spherical inhomogeneity derived in this way was lower by about 5%, whereas the reduced scattering coefficient was determined to be larger by 10% compared with the values used in the forward simulations. These differences in the optical properties of the sphere are about the same as the uncertainties for the optical properties of the base materials. Furthermore, the 10% increase of the reduced scattering coefficient caused by neglecting Fresnel reflections at the surface of the spheres essentially compensates for the small difference in the nominal values of the reduced scattering coefficients of the spheres (12.1 cm^{-1}) and of the surrounding scattering solution (13.0 cm^{-1}). It follows that within experimental uncertainties both spherical inhomogeneities contained in our phantom represent pure absorbers.

3.2. Pre-processing of phantom data

Each distribution of times of flight $N(t)$ was recorded at a time resolution (bin size) of 16.276 ps. After correction for background counts, distributions of times of flight of photons were Fourier transformed into frequency domain and the complex discrete Fourier amplitudes $\hat{N}(\omega)$ were taken at the sampling frequency of $\omega_0/2\pi = 126.2 \text{ MHz}$. Subsequently raw logarithmic data $w_{\text{R}}(\omega_0) = \ln\{\hat{N}(\omega_0)/\hat{N}_0(\omega_0)\}$ were generated. The complex amplitudes

$\hat{N}_0(\omega_0)$ used for normalization were calculated from DTOFs measured at source–detector positions at which the influence of the absorbing spheres of the phantom could be neglected ($N_0(t) = N(t)$). Subsequently, the 2D discrete spatial Fourier transforms $\tilde{w}_R(\omega_0)$ were calculated from $w_R(\omega_0)$ for each offset $\delta\vec{\rho}$ (cf equation (17)), and only the nine ‘lowest’ spatial frequencies ($N_{\ell p} = M_{\ell p} = 9$, see section 2.2.2) were taken into account in the reconstruction of the optical properties. Figure 2 illustrates this filtering for offsets $\delta\vec{\rho} = (0, 0)$, (left-hand column) and $\delta\vec{\rho} = (5 \text{ cm}, 0)$, (right-hand column), depicting fields of view (FOV) in the detector plane of 25×25 pixels ($-3 \text{ cm} \leq x_D, y_D \leq 3 \text{ cm}$) and 45×25 pixels ($-8 \text{ cm} \leq x_D \leq 3 \text{ cm}, -3 \text{ cm} \leq y_D \leq 3 \text{ cm}$), respectively, viewed from the detector. The upper half of figure 2 displays real parts, the lower half imaginary parts of logarithmic data in real space, i.e. of raw experimental data $w_R(\omega_0)$ (figures 2(a) and (e)), and low-pass filtered experimental data $w_R^{\text{lpf}}(\omega_0)$ (figures 2(b) and (f)), obtained from equation (28) taking only the nine ‘lowest’ spatial frequencies (see above) into account in the inverse discrete Fourier transformation. Figures 2(c), (d) and (g), (h) represent simulated data $w_R^{\text{sim}}(\omega_0)$, based on the same forward models which were used in the reconstruction of optical properties. The simulated data $w_R^{\text{sim}}(\omega_0)$ were obtained from equation (29), where the kernels K_a and K_D were calculated according to equations (13), (18) using the Green’s function G_0^{slab} and spectral photon density \hat{u}_0 for the infinite slab (figures 2(c), (g)) or the Green’s function G_0^{inf} and spectral photon density \hat{u}_0 for the infinite medium (figures 2(d), (h)), the known locations of the 1 cm diameter spherical inhomogeneities, their known optical properties $\mu'_{s,\text{sph}}, \mu_{a,\text{sph}}$ and the known background optical properties μ'_{s0}, μ_{a0} . Filtering of the experimental data removes excessive noise originating from higher spatial frequencies, as can be seen by comparing figures 2(a) and (b), without significant loss of spatial resolution. Furthermore, simulated data (figures 2(c), (d)) agree well with the filtered experimental data (figure 2(b)) with respect to spatial distribution. However, whereas simulated data based on the infinite medium as the model agree almost quantitatively with the experimental data, simulated data based on the more realistic infinite slab model are larger by a factor of about 2.5 (cf figures 2(c), (b)). We attribute the latter discrepancy to limitations of linear perturbation theory. When analysing experimental data by linear perturbation theory changes in the absorption coefficient of absorbers from the background value tend to be underestimated. Conversely, differences between experimental and simulated data are overestimated by linear perturbation theory when the true absorption changes are used. Apparently, when adopting the infinite medium model, the various approximations made compensate each other. However, further studies are needed to clarify this point.

Since both inhomogeneities are pure absorbers, phase changes are expected to be small. Therefore, the real part of the logarithmic data corresponds to a change in demodulation (damping) of photon density waves, whereas the imaginary part is proportional to phase changes with respect to the homogeneous medium. This is borne out by the lower part of figure 2. Only (phase) noise is seen in the raw experimental data (figure 2(e)), whereas the filtered experimental data (left column, figure 2(f)) exhibit a pattern of (phase) changes that shows some similarity with the simulated patterns. However, it should be kept in mind that the mismatch in index of refraction between the solid spheres and the dilute milk was not taken into account in the simulations.

As discussed above (cf section 2.2.2) *in vivo* data must be normalized differently, since generally ‘unperturbed’ data $N_0(t)$ cannot be obtained in this case. We have chosen to use the complex Fourier amplitudes $\hat{N}_0^{\text{ave}}(\omega_0)$ (cf equation (26)) to normalize *in vivo* data, averaged over all Fourier amplitudes $\hat{N}(\omega_0)$ corresponding to the same offset. In order to investigate the influence of this approximation we compared the logarithmic data shown in figures 2(a), (e) and (b), (f) with the real and imaginary parts of logarithmic (raw) data

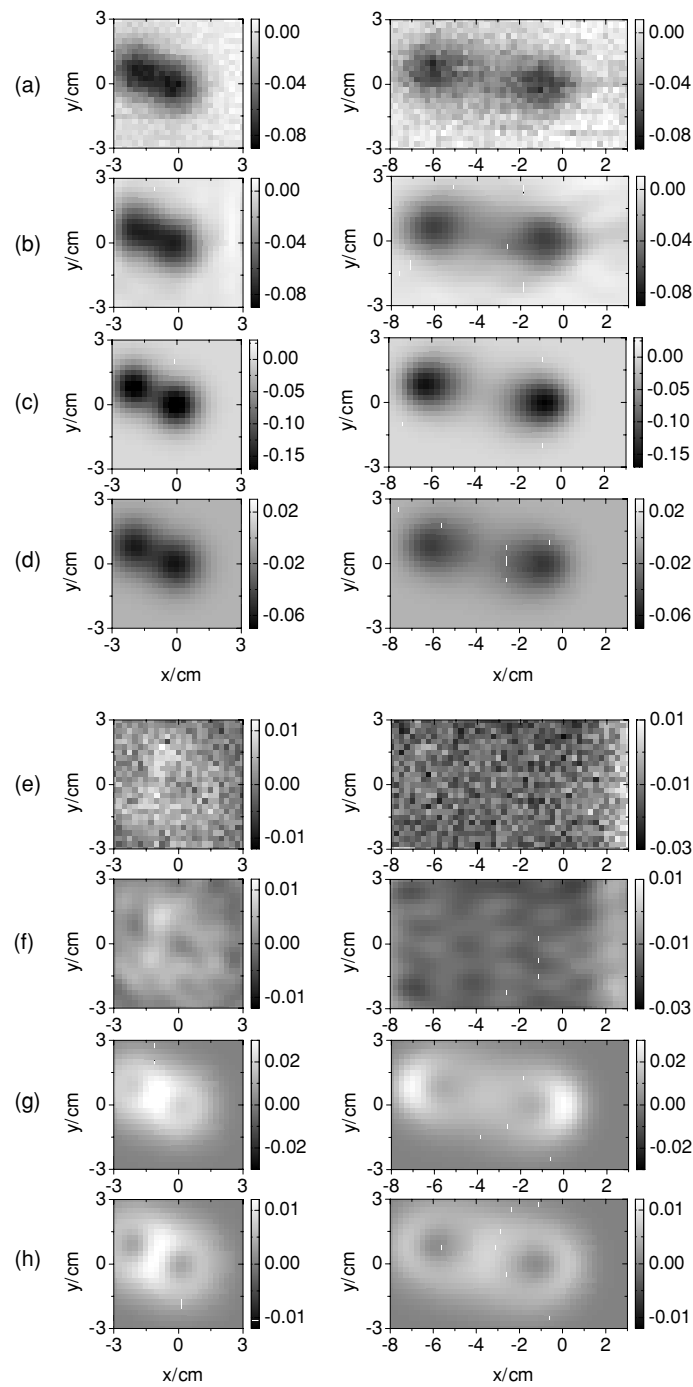


Figure 2. Effect of k space filtering for the phantom (cf figure 1) with two absorbing spheres; (a)–(d) real part and (e)–(h) imaginary part of logarithmic data $w_R(x, y)$ (cf equations (27)–(29)), normalized to homogeneous phantom data (local average); (a), (e) raw data (measurement), (b), (f) measured data after k space filtering; (c), (g) simulated data for the infinite slab model; (d), (h) simulated data for the infinite medium model; left column corresponds to source detector offset $\Delta x_D = 0$, right column to $\Delta x_D = +5$ cm.

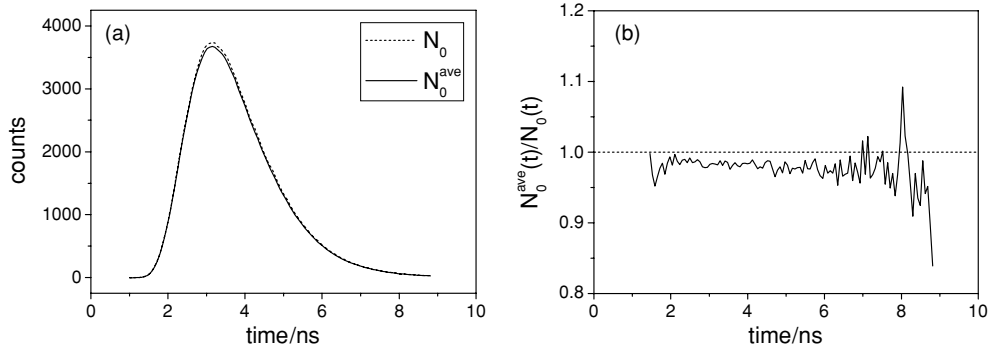


Figure 3. Distribution of times of flight of photons $N_0(t)$ (local average, dashed line) recorded in transmission at zero source–detector offset through homogeneous phantom and $N_0^{\text{ave}}(t)$ (global average, solid line) obtained as average over all distributions of times of flight $N(t)$ through heterogeneous phantom at zero offset (a); ratio $N_0^{\text{ave}}(t)/N_0(t)$ (b).

$w_{\text{R}}^{\text{ave}}(\omega_0) = \ln \{ \hat{N}(\omega_0) / \hat{N}_0^{\text{ave}}(\omega_0) \}$ (cf equation (27)) and corresponding low-pass filtered data $w_{\text{R}}^{\text{ave}, \ell\text{pf}}(\omega_0)$ derived from our phantom measurements. Corresponding images are virtually identical, i.e. independent of normalization, apart from a shift of scale. For example, as can be seen from figures 2(a) and (b), shown in the left column, $\text{Re}\{w_{\text{R}}(\omega_0)\} \approx 0.0$ for areas sufficiently far from the absorbers, whereas a value of $\text{Re}\{w_{\text{R}}^{\text{ave}}(\omega_0)\} \approx 0.02$ was obtained for the same areas when normalizing to $\hat{N}_0^{\text{ave}}(\omega_0)$. This shift of scale is to be expected since absorption of the spheres reduces the complex Fourier amplitude $\hat{N}_0^{\text{ave}}(\omega_0)$ compared to $\hat{N}_0(\omega_0)$, i.e. $|\hat{N}_0^{\text{ave}}(\omega_0) / \hat{N}_0(\omega_0)| < 1$. For illustration figure 3 compares the unperturbed DTOF $N_0(t)$ and the distribution of times of flight of photons $N_0^{\text{ave}}(t)$ obtained by averaging all measured DTOFs $N(t)$ corresponding to the same (zero) source–detector offset ($\delta\vec{\rho} = (0,0)$). Both DTOFs, $N_0(t)$ and $N_0^{\text{ave}}(t)$, have the same shape but slightly different amplitudes. This is to be expected, since it is well known that for absorbing objects the temporal point spread function of the heterogeneous medium is unchanged apart from a reduction in its amplitude due to attenuation (Gandjbakhche *et al* 1998). Since background optical properties are derived from the shape only of the distributions of times of flight, $N_0(t)$ and $N_0^{\text{ave}}(t)$ yield the same values for $\mu'_{\text{s}0}$ and $\mu_{\text{a}0}$. Although the amplitudes differ by only a few per cent in the present case (see figure 3), the choice of normalization has a remarkable influence on the reconstruction of the absorption coefficient, discussed in the next section. In the following we refer to $w_{\text{R}}(\omega_0)$, $w_{\text{R}}^{\ell\text{pf}}(\omega_0)$ as properly normalized and to $w_{\text{R}}^{\text{ave}}(\omega_0)$, $w_{\text{R}}^{\text{ave}, \ell\text{pf}}(\omega_0)$ as approximately normalized logarithmic data.

4. Reconstructed phantom optical properties

4.1. Reconstruction of absorption coefficient only

For reconstruction of the optical properties of the phantom, we selected the volume $-3.3 \text{ cm} \leq x, y \leq 3.3 \text{ cm}$, $0 \leq z \leq 6 \text{ cm}$ and divided it into $N_{\text{vox}} = 1210$ voxels of volume $\Delta V = 0.6 \times 0.6 \times 0.6 \text{ cm}^3$. Since both spherical inhomogeneities can be treated as pure absorbers, we reconstructed the change $\delta\mu_{\text{a}}(\vec{r})$ in the absorption coefficient from the background value $\mu_{\text{a}0}$ setting at the same time $\delta D(\vec{r}) = 0$. The model of an infinite slab was adopted, i.e. the kernel $K_{\text{a}}^{\text{slab}}$ (equations (13), (16)) was calculated using the Green's function G_0^{slab} (equation (11)) and the spectral photon density \hat{u}_0 for an infinite homogeneous slab. Absorption coefficients were reconstructed both from properly normalized

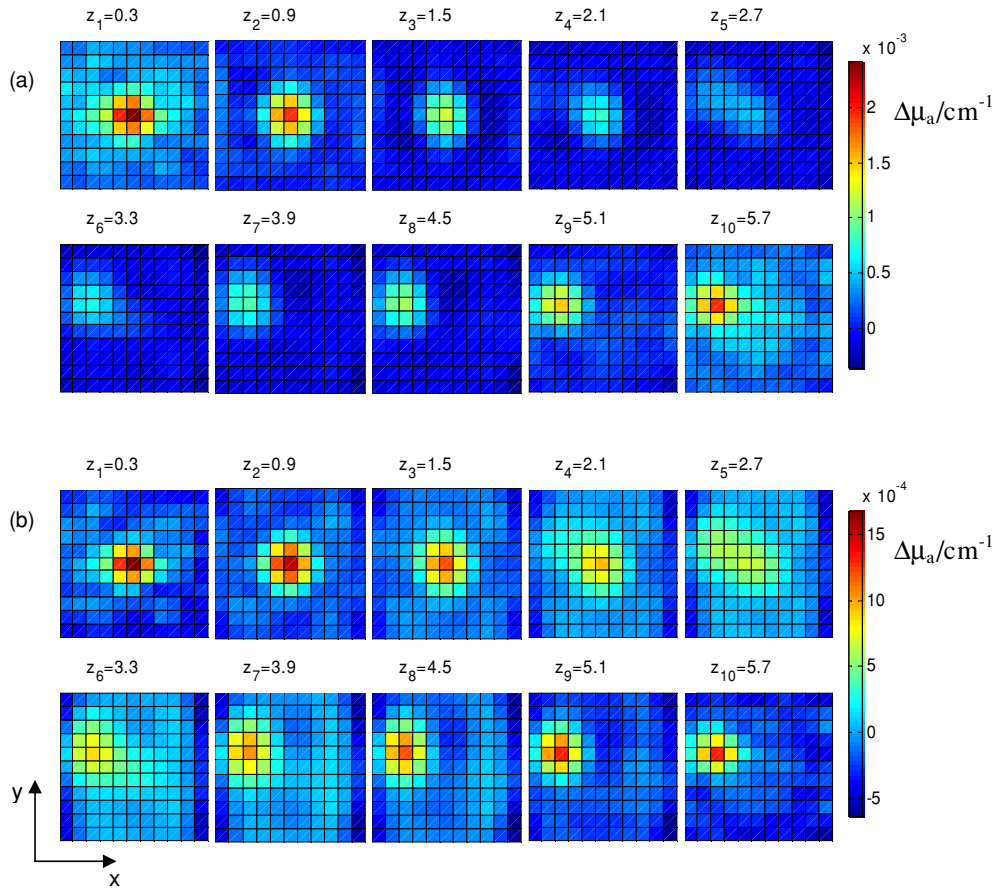


Figure 4. Reconstructed changes in absorption coefficient of phantom in ten contiguous slices parallel to source and detector plane at distances z_i cm from source plane ($z = 0$) from properly normalized (a) and approximately normalized (b) logarithmic data using Green's function for infinite slab (regularization parameter $\alpha = 10^3$) and assuming $\delta D = 0$; orientation of axes is indicated in lower left corner (cf figure 1).

($\tilde{w}_R^{\ell\text{pf}}(\omega_0)$) and approximately normalized ($\tilde{w}_R^{\text{ave},\ell\text{pf}}(\omega_0)$) logarithmic data transformed into Fourier space and low-pass filtered taking the nine lowest spatial frequencies (see section 3.2) into account only. Thus, absorption coefficients were reconstructed from a total of $N_{\text{meas}} = N_{\text{off}} \times N_{\ell\text{p}} \times M_{\ell\text{p}} = N_{\text{off}} \times 9 \times 9$ complex data points. Reconstructions were carried out for various assumed values of the regularization parameter α , and, generally, the lowest value of α was selected that provided an acceptable contrast to noise ratio in the reconstructed images. Figure 4 which displays $\delta\mu_a(z_i)$ in ten contiguous slices ($i = 1, \dots, 10$) parallel to the source plane ($z = 0$) and detector plane ($z = 6$ cm), illustrates the results obtained ($\alpha = 10^3$) from $N_{\text{meas}} = 405$ properly (figure 4(a)) and approximately (figure 4(b)) normalized complex data points when the five source–detector offsets $\Delta x_D = 0, \pm 2, \pm 5$ cm were included in the reconstruction. As can be seen from figure 4(a), the two inhomogeneities can be clearly distinguished and both spheres appear at their correct lateral positions, ($x_1^{\text{sph}} = -2$ cm, $y_1^{\text{sph}} = 0.85$ cm and $x_2^{\text{sph}} = y_2^{\text{sph}} = 0$ cm). Because of the limited span of projection angles (paraxial data) used, the reconstructed depths of the absorbing spheres are smeared out along the z -axis to some extent, and the centres of gravity of $\delta\mu_a(\vec{r})$ appear to be

located closer to the source and detector planes, respectively, compared to the true positions. Smearing out of the reconstructed absorption coefficient is clearly worse, i.e. longitudinal resolution significantly lower, when approximately normalized logarithmic data are used in the reconstruction (figure 4(b)). The results shown in figure 4 were not improved significantly, when all 11 source–detector offsets were included in the analysis. Furthermore, the maximum of the reconstructed change in the absorption coefficient ($\delta\mu_{a,\max}^{\text{recon}} \approx 0.0025 \text{ cm}^{-1}$, see figure 4(a)) is lower than expected, since $\delta\mu_a(\vec{r})$ is smeared out along the z -axis. We note in passing that qualitatively the same results were obtained when an infinite medium was assumed ($\alpha = 10^2$) rather than an infinite slab to represent the compressed breast, i.e. when the kernel K_a^{inf} was calculated from the Green's function G_0^{inf} and spectral photon density \hat{u}_0 for the infinite medium. In this case the reconstructed centres of gravity of $\delta\mu_a(\vec{r})$ along the z -axis deviate from the true positions z_1^{sph} and z_2^{sph} even further, whereas the maximum $\delta\mu_{a,\max}^{\text{recon}} \approx 0.005 \text{ cm}^{-1}$ of the reconstructed change in absorption is somewhat closer to the experimental value.

4.2. Simultaneous reconstruction of absorption and diffusion coefficients

Prior knowledge of the difference in the scattering coefficients between a lesion and surrounding breast tissue is generally not available. Therefore, we additionally reconstructed the change in the absorption $\delta\mu_a(\vec{r})$ and diffusion $\delta D(\vec{r})$ coefficients simultaneously from properly normalized logarithmic phantom data ($\tilde{w}_R^{\text{lpf}}(\omega_0)$) using the kernels $K_a^{\text{slab}}, K_D^{\text{slab}}$ for the infinite slab (figure 5) and $K_a^{\text{inf}}, K_D^{\text{inf}}$ for the infinite medium (figure 6), respectively, with regularization parameter chosen to be $\alpha = 10^3$ (slab) and $\alpha = 10^2$ (infinite medium). As can be seen from figure 5(a), in the reconstructed absorption image both spheres can no longer be separated along the z direction, when adopting the homogeneous infinite slab as the model. As before, spatial resolution along the z -axis is even further compromised when optical properties were reconstructed from approximately normalized data ($\tilde{w}_R^{\text{ave,lpf}}(\omega_0)$). However, when the kernels $K_a^{\text{inf}}, K_D^{\text{inf}}$ are used in the reconstruction, both spherical objects are well separated along the z direction in the absorption image (figure 6(a)). When prior knowledge about the phantom (pure absorbing spheres) is not taken into account, the infinite medium model provides better identification of both inhomogeneities compared to the infinite slab, although the latter model is closer to reality. This result is in line with our observation made that the infinite medium model apparently provides better agreement between simulated ($w_R^{\text{sim}}(\omega_0)$) and low-pass filtered ($w_R^{\text{lpf}}(\omega_0)$) experimental logarithmic phantom data (cf figures 2(b) and (d)), but needs further investigations for clarification. As can be seen from figure 6(a) both spheres appear too close to the source and detector plane, respectively, compared to their true locations, as was observed when only the absorption coefficient $\delta\mu_a(\vec{r})$ was reconstructed from phantom data using both the infinite slab and infinite medium as the model. Furthermore, both inhomogeneities show up in the reconstructed scattering images of figures 5 and 6 because of cross-talk.

5. Recording of *in vivo* paraxial optical mammograms

5.1. Scanning time-domain paraxial optical mammograph

We used a four (detection-)channel scanning time-domain optical mammograph to record paraxial optical mammograms of a patient with a mastopathy in her left breast. Distributions of times of flight of photons were measured through the breast slightly compressed between two parallel glass plates along the craniocaudal projection direction. As light sources, four

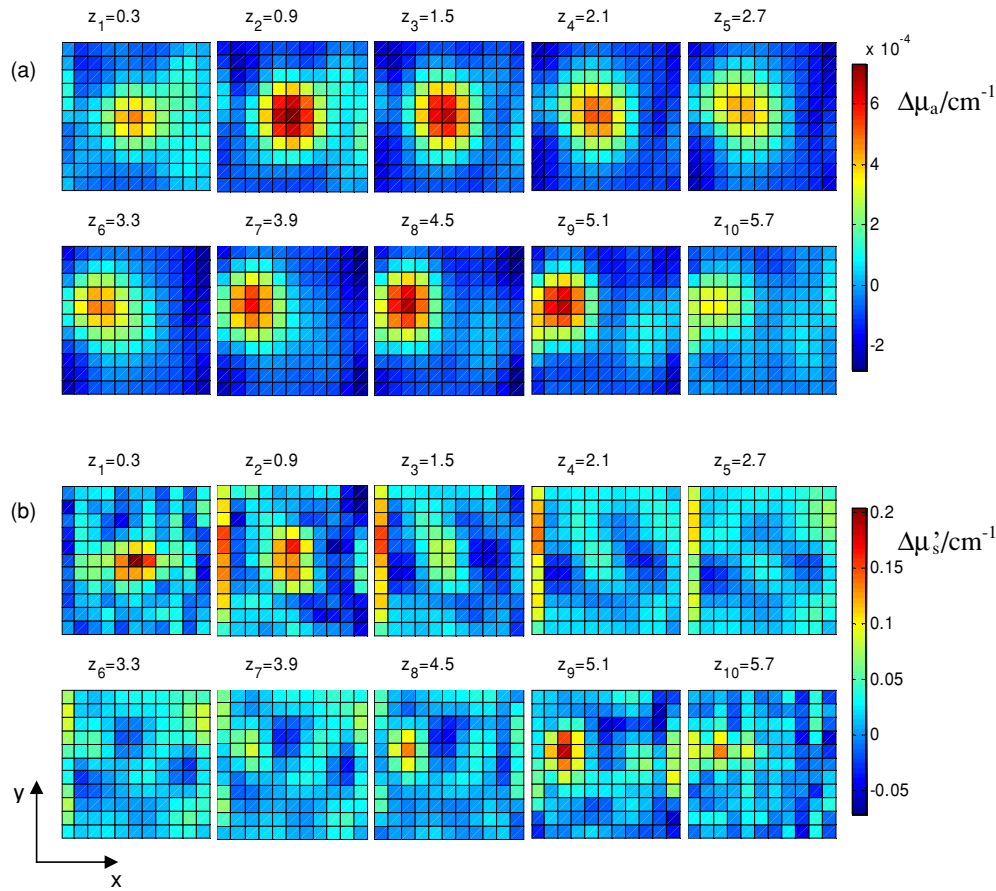


Figure 5. Changes in absorption (a) and reduced scattering (b) coefficient of phantom in ten contiguous slices (cf figure 4(a)) simultaneously reconstructed from properly normalized logarithmic data using Green's function of infinite slab ($\alpha = 10^3$); orientation of axes is indicated in lower left corner (cf figure 1).

picosecond diode lasers were used, emitting at 652 nm, 684 nm, 797 nm and 830 nm. The diode laser outputs were interlaced in time and coupled into an optical fibre. The transmitting fibre and the four receiving fibre bundles which correspond to four fixed source–detector offsets $\delta\vec{\rho} = (0, 0)$, $\delta\vec{\rho} = (\pm 2 \text{ cm}, 0)$ and $\delta\vec{\rho} = (0, 2 \text{ cm})$ were scanned in tandem across the breast in a meandering fashion. To this end the transmitting fibre together with the four detecting fibre bundles moved continuously along the x -axis (parallel to the chest wall), covering $\Delta x_{\text{step}} = 0.25 \text{ cm}$ in about 150 ms; neighbouring scans were separated by $\Delta y_{\text{step}} = 0.25 \text{ cm}$. Time-correlated single photon counting was carried out during each of the 150 ms intervals at count rates up to 1 MHz. Each fibre bundle was connected to a separate detection module. Further details on the instrument, on the recording of mammograms and on measurements of the instrumental response function are given in another contribution of the present issue (Grosenick *et al* 2005).

5.2. Generation of optical mammograms from recorded temporal point spread functions

5.2.1. Time-window analysis.

Optical mammograms were generated from measured distributions of times of flight of photons (temporal point spread functions) by time-window

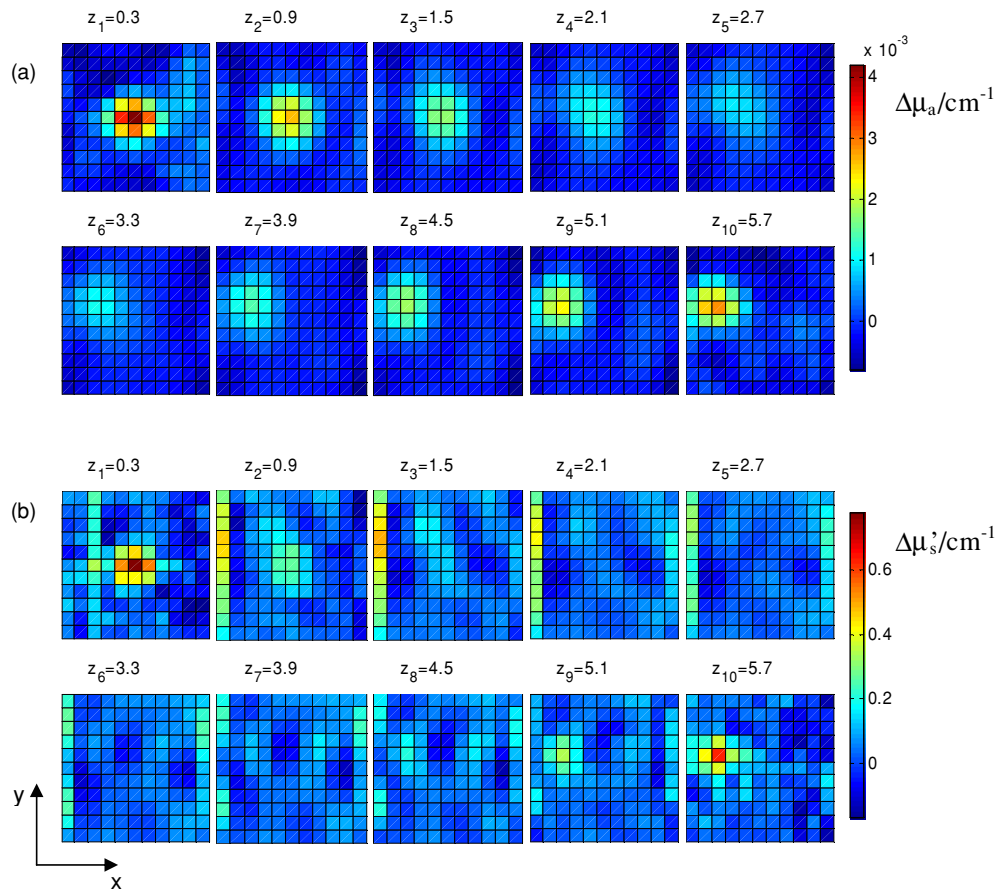


Figure 6. Changes of absorption (a) and reduced scattering (b) coefficient of phantom in ten contiguous slices simultaneously reconstructed from properly normalized logarithmic data using Green's function of the infinite medium ($\alpha = 10^2$); orientation of axes is indicated in lower left corner (cf figure 1).

analysis, e.g. by calculating photon counts (N_g) in a late time window (Grosenick *et al* 1999, 2005). Mammograms obtained in this way essentially display absorption contrast. For illustration, figure 7 shows mammograms ($\lambda = 652$ nm) of a patient known to carry a mastopathy in her left breast. The lesion, indicated by an arrow labelled 'M', appears at $x_M = -2.0$ cm, $y_M = 1.5$ cm at zero source–detector offset (figure 7(a)) and shifts to positions $x_M = 0$ cm, $y_M = 1.5$ cm (figure 7(b)) and $x_M = -4.0$ cm, $y_M = 1.5$ cm (figure 7(c)) for offsets $\delta\vec{\rho} = (-2$ cm, 0) and $\delta\vec{\rho} = (2$ cm, 0), respectively, indicating that the lesion is situated in the lower part (detector side) of the breast. There is another area of reduced transmittance (arrow 'G') centred at $x_G = -0.5$ cm, $y_G = 1.0$ cm (figures 7(a), (c)) caused either by glandular tissue or by mastopathic alterations. This area which, too, is close to the breast wall partially overlaps in the projection mammograms with the mastopathy in the lower part of the breast and appears on the right-hand side of the mastopathy. Since this area does not shift with source–detector offset ($\delta\vec{\rho} \neq 0$) it is located in the upper part of the breast (source side). Furthermore, at the lower left corner of the mammograms there is an area (arrow 'F') of high transmittance ($x_F = -5$ cm, $y_F = 1$ cm, figure 7(a)) which shifts to the right-hand side ($x_F = -4$ cm, $y_F = 1$ cm, figure 7(b)) for negative source–detector offset ($\delta\vec{\rho} = (-2$ cm, 0)) and to the left-hand side

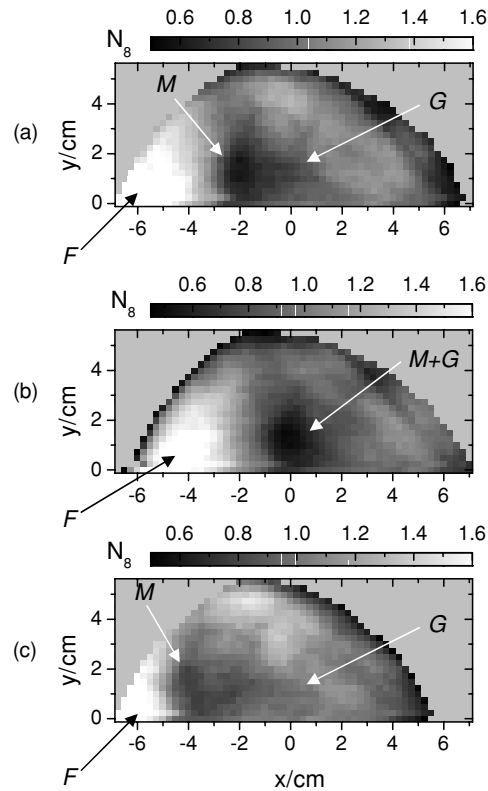


Figure 7. Craniocaudal projection optical ($\lambda = 652$ nm) mammograms (left breast) of patient with mastopathy displaying normalized photon counts N_8 in a late time window; (a) offset $\delta\vec{\rho} = (0, 0)$; (b) $\delta\vec{\rho} = (\Delta x_D = -2$ cm, 0), (c) $\delta\vec{\rho} = (\Delta x_D = +2$ cm, 0); arrows point to inhomogeneities associated with mastopathy (M), glandular tissue (G) and fat (F).

($x_F = -6$ cm, $y_F = 1$ cm) for positive offset ($\delta\vec{\rho} = (2$ cm, 0)). For the same source–detector offset, the shift of this area is only half of that experienced by the mastopathy and, therefore, the volume identified as fatty tissue because of its high transmittance is situated about halfway between both compression plates.

5.2.2. Homogeneous optical properties. Although time-window analysis provides for model-free generation of optical mammograms, for a more direct comparison with reconstructed absorption and reduced scattering coefficients, we generated optical projection mammograms by deriving homogeneous (average) absorption $\mu_{a,\text{hom}}$ and reduced scattering $\mu'_{s,\text{hom}}$ coefficients from measured distributions of times of flight of photons $N(t)$. To this end at each scan position the compressed breast was modelled as infinite homogeneous slab of thickness d derived from the first moment of $N(t)$ corresponding to the particular scan position (Grosenick *et al* 2003). Subsequently, the analytical solution of the diffusion equation for the photon flux density through a homogeneous infinite slab of thickness d assuming extrapolated boundary conditions was convolved with the measured instrumental response function and fitted to $N(t)$ within a two-step minimization procedure (Grosenick *et al* 2003) to obtain $\mu_{a,\text{hom}}$ and $\mu'_{s,\text{hom}}$ for the particular scan position. Figure 8 shows mammograms at zero offset $\delta\vec{\rho} = (0, 0)$ (figures 8(a), (b)) and negative offset $\delta\vec{\rho} = (-2$ cm, 0) (figures 8(c), (d))

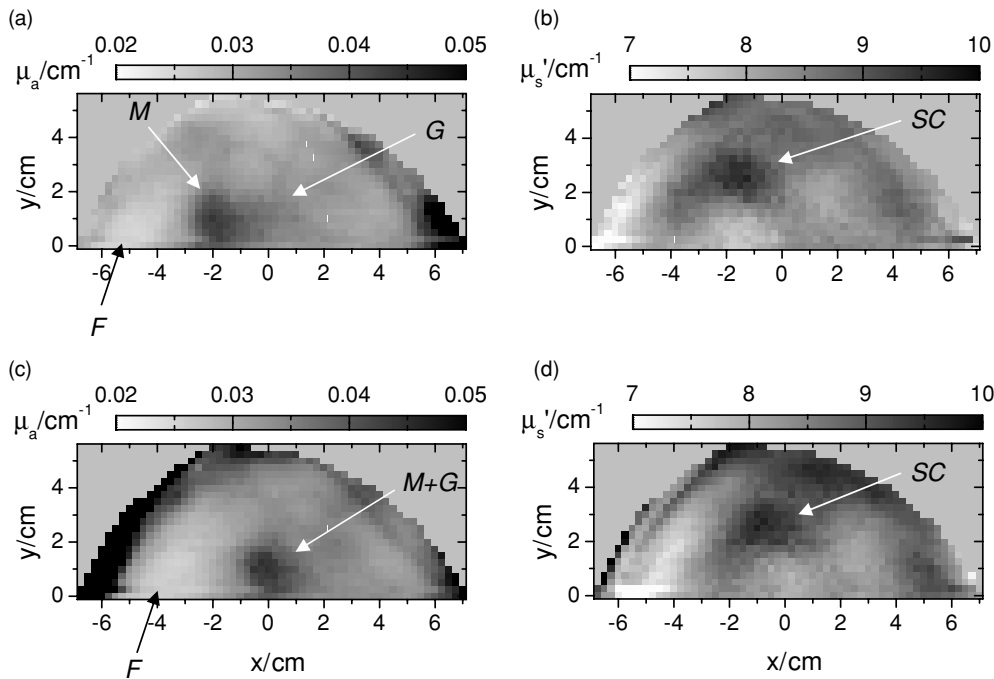


Figure 8. Optical mammograms displaying average absorption and reduced scattering coefficients obtained from the model of homogeneous slab; (a) absorption coefficient at offset $\delta\vec{\rho} = (0, 0)$; (b) reduced scattering coefficient at offset $\delta\vec{\rho} = (0, 0)$; (c) absorption coefficient at offset $\delta\vec{\rho} = (-2 \text{ cm}, 0)$; (d) reduced scattering coefficient at offset $\delta\vec{\rho} = (-2 \text{ cm}, 0)$; arrows in absorption images point to the same inhomogeneities as in figure 7, in scattering image arrow (SC) points to unidentified inhomogeneity.

displaying average absorption (figures 8(a), (c)) and reduced scattering (figures 8(b), (d)) coefficients obtained in this way. It should be noted that the projection mammograms shown in figures 7 and 8 were derived from the same data set. The absorption mammogram of figure 8(a) shows the mastopathy (cf arrow M) at $x_M = -2.0 \text{ cm}$, $y_M = 1.0 \text{ cm}$, the area of reduced transmittance (cf arrow G) on its right-hand side at $x_G = -0.75 \text{ cm}$, $y_G = 1.0 \text{ cm}$, and the area of increased transmittance (arrow F) at the lower left corner at $x_F = -5 \text{ cm}$, $y_F = 1 \text{ cm}$. On the other hand, the scattering mammogram (figure 8(b)) shows an area of increased scattering (arrow ‘SC’) at $x = -1.8 \text{ cm}$, $y = 2.7 \text{ cm}$, just above the mastopathy. This area is absent from the absorption image (figure 8(a)) and extends the mastopathy in figure 7(a) to larger y values (i.e. further to the nipple). At present we cannot correlate the area of increased scattering with a specific tissue compartment. In the mammograms recorded at negative source–detector offset the mastopathy shifts to $x_M = -0.25 \text{ cm}$, $y_M = 1.0 \text{ cm}$ (figure 8(c)), consistent with the discussion of figure 7, and the area of increased scattering to $x = -0.8 \text{ cm}$, $y = 2.7 \text{ cm}$ (figure 8(d)), indicating that the corresponding tissue volume is situated about halfway between the compression plates (middle plane of the breast).

5.3. Pre-processing of *in vivo* data for image reconstruction

For reconstruction of absorption $\mu_a(\vec{r}) = \mu_{a,\text{global}} + \delta\mu_a(\vec{r})$ and reduced scattering coefficients $\mu'_s(\vec{r}) = \mu'_{s,\text{global}} + \delta\mu'_s(\vec{r})$ from the mammograms recorded at various source–detector offsets $\delta\vec{\rho}$, background optical properties $\mu_{a,\text{global}}$ and $\mu'_{s,\text{global}}$ are needed. To derive background

optical properties an average distribution of times of flight of photons $N_{\text{ave,global}}(t)$ was calculated for each mammogram by taking the average over all distributions $N(t)$ with first moments exceeding the median of all first moments associated with the particular mammogram (Grosenick *et al* 2003). In this way the outer parts of the compressed breast which did not fill the gap between both glass plates are not taken into account when calculating $N_{\text{ave,global}}(t)$. From $N_{\text{ave,global}}(t)$ background optical properties $\mu_{\text{a,global}}$, and $\mu'_{\text{s,global}}$ were deduced in a similar way as described above (see section 5.2.2). Finally, the background optical properties deduced from the four offset mammograms ($\lambda = 652$ nm) were averaged to obtain $\mu_{\text{a,global}} = (0.034 \pm 0.003) \text{ cm}^{-1}$ and $\mu'_{\text{s,global}} = (8.2 \pm 0.8) \text{ cm}^{-1}$.

Each DTOF $N(t)$ was recorded at a time resolution (bin size) of 48.86 ps. After correction for background counts, DTOFs were Fourier transformed into frequency domain and the complex discrete Fourier amplitude $\hat{N}(\omega)$ was taken at the sampling frequency of $\omega_0/2\pi = 90.6$ MHz. Subsequently, the average $\hat{N}_0^{\text{ave}}(\omega_0)$ of all Fourier amplitudes $\hat{N}(\omega_0)$ corresponding to the same offset $\delta\vec{\rho}$ was calculated (see equation (26)) and used to generate the (raw) data vector $w_{\text{R}}^{\text{ave}}(\omega_0) = \ln \{ \hat{N}(\omega_0) / \hat{N}_0^{\text{ave}}(\omega_0) \}$ as described above (see equation (27)). As can be seen from figure 7, the x -scan closest to the chest wall ($y_{\text{S}} = 0$) extended from $x_{\text{S}} = -6.75$ cm up to $x_{\text{S}} = 7$ cm, sampling 56 scan positions. However, x -scans further away from the chest wall covered a smaller range and, prior to 2D discrete Fourier transformation, the number of scan positions sampled was increased to 56 in each case by zero padding, yielding a total of $N_{\text{step}} \times M_{\text{step}} = 56 \times 23 = 1288$ source locations. The 2D discrete Fourier transforms $\tilde{w}_{\text{R}}^{\text{ave}}(\omega_0)$ were calculated from $w_{\text{R}}^{\text{ave}}(\omega_0)$, taking only the $N_{\ell_{\text{p}}} = M_{\ell_{\text{p}}} = 9$ 'lowest' spatial frequencies into account (see section 2.2.2). It follows that the absorption and reduced scattering coefficient were reconstructed from $N_{\text{meas}} = 4 \times 9 \times 9 = 324$ complex data points.

6. Reconstructed absorption and reduced scattering coefficients of breast tissue *in vivo*

For simultaneously reconstructing changes $\delta\mu_{\text{a}}(\vec{r})$ and $\delta\mu'_{\text{s}}(\vec{r})$ in the absorption and reduced scattering coefficients from the global background optical properties $\mu_{\text{a,global}}$, $\mu'_{\text{s,global}}$, we chose a homogeneous infinite slab of thickness d_{gap} as the (background) model for the compressed breast. However, since breast thickness decreases towards its outer parts the volume of breast tissue selected for reconstruction ($-5.75 \text{ cm} \leq x \leq 5.75 \text{ cm}$, $-0.25 \text{ cm} \leq y \leq 4.75 \text{ cm}$, $0 \leq z \leq 5.6 \text{ cm}$) was somewhat smaller than the rectangular volume, covered by the x , y scans of the mammograph after zero padding. The volume selected for reconstruction was divided into $N_{\text{vox}} = 1840$ voxels of volume $\Delta V = h_x \times h_y \times h_z = 0.5 \text{ cm} \times 0.5 \text{ cm} \times 0.7 \text{ cm}$. The results ($\alpha = 10^4$) obtained from the four offset optical mammograms ($\lambda = 652$ nm) are shown in figures 9(a) and (b), corresponding to absorption and reduced scattering images, respectively, depicting $\delta\mu_{\text{a}}(z_i)$ and $\delta\mu'_{\text{s}}(z_i)$ in eight contiguous slices ($i = 1 \dots 8$) parallel to the source plane ($z = 0$) and detector plane ($z = 5.6$ cm), separated by 0.7 cm. Although the reconstructed area in the x , y plane is somewhat smaller than the true size of the breast (see above) its rounded shape can be identified in figures 9(a), (b) by the low values of the reconstructed changes in the absorption ($\delta\mu_{\text{a}}(z_i)$) and reduced scattering ($\delta\mu'_{\text{s}}(z_i)$) coefficient, respectively. Large values of $\delta\mu_{\text{a}}(z_i)$ and $\delta\mu'_{\text{s}}(z_i)$ beyond the rounded boundaries are probably artefacts of the reconstruction.

In all slices of figure 9(a), there appears an area of increased absorption that protrudes from the chest wall. The shape of this area changes from slice to slice; it is of semicircular shape at the top but more localized and shifted to the left at the bottom. The latter area coincides with the location of the mastopathy, known to be on the lower side of the breast. From the reconstruction of the optical properties of the phantom containing two absorbing

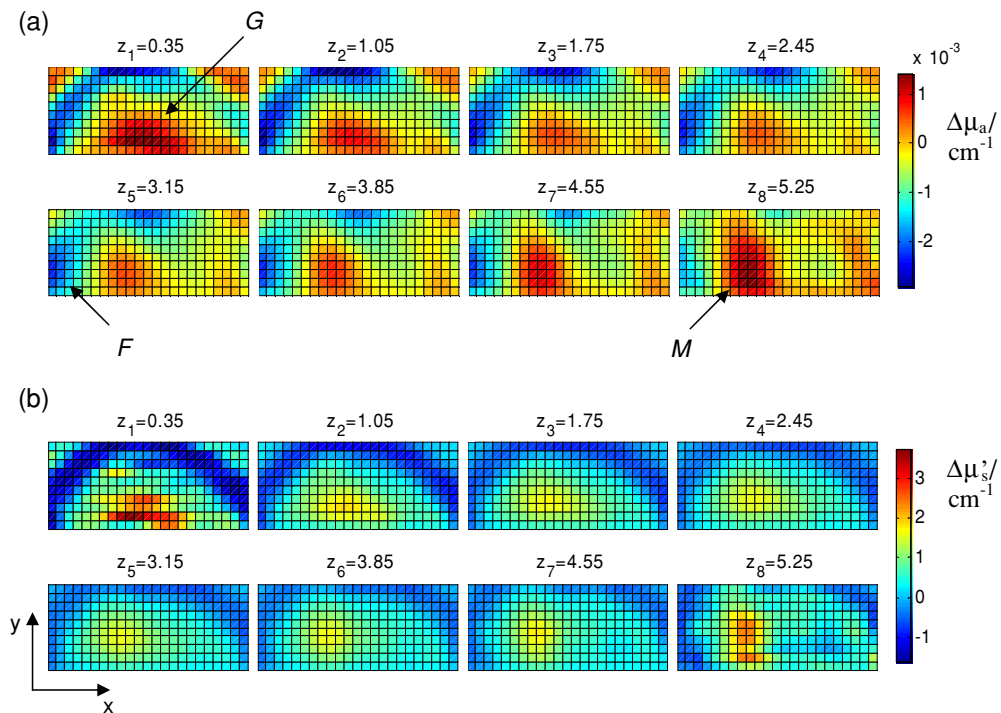


Figure 9. Absorption (a) and reduced scattering (b) coefficients, simultaneously reconstructed from approximately normalized patient data (cf figures 7 and 8) using Green's function of the infinite slab ($\alpha = 10^4$) in eight contiguous slices parallel to the compression plates at distances of z_i cm from the top plate. Arrows point to the same inhomogeneities as in figures 7 and 8.

spheres using the infinite slab model, we know that the limited angular (paraxial) data cause considerable smearing out of the location of both absorbers. The same is to be expected when reconstructing the optical properties of the breast, in particular since the angular span covered by the *in vivo* measurements is even smaller. However, comparing figures 5(a) and 9(a), a similar change in the shape of the reconstructed absorption coefficient occurs from slice to slice in either case. From the reconstructed absorption coefficient of the phantom, the two absorbing spheres located in different slices could not be distinguished from an elongated tilted object. Likewise in the *in vivo* case we cannot decide whether the volume of the absorbing tissue, located in the upper part and centred at $x_G = -0.5$ cm, $y = 1.0$ cm (see arrow G in figures 7(a), 9(a)) is separated from the mastopathy (see arrow M in figures 7(a), 9(a)) at the bottom of the breast, or whether these tissue compartments (glandular tissue, mastopathy) extend over the thickness of the compressed breast. Furthermore, the area of high transmittance (fatty tissue) located in the lower left corner (arrow F) of figure 7(a) can be identified on the lower left side of all slices shown in figure 9(a).

In all slices of figure 9(b), there appears a scattering inhomogeneity the position of which coincides with the position of the mastopathy and of the scattering inhomogeneity visible in figure 8(b). However it should be kept in mind that cross-talk between the absorption and scattering images is likely to occur, as was observed for the phantom. As a matter of fact the change in the shape of the reduced scattering coefficient from slice to slice seen in figure 9(b) mimics the changes in the shape of the absorption coefficient of figure 9(a). Furthermore, according to figure 8(a) the mastopathy seems to be predominantly an absorbing object and

the scattering inhomogeneity (arrow SC) of figure 8(b) is located close to the centre plane of the compressed breast, rather than at its lower side. It follows that figure 9(b) more likely reflects cross-talk between absorption and scattering than the true scattering properties of the tissue. Essentially the same conclusions were reached when the absorption coefficient or reduced scattering coefficient were reconstructed separately. Furthermore, apart from the regularization parameter α selected, qualitatively the same results were obtained when using an infinite medium as the model for the compressed breast for the reconstruction, rather than the infinite slab.

7. Conclusions

We presented a computationally efficient method for solving the inverse problem associated with scanning paraxial time-domain optical mammography. Our reconstruction method which uses the Rytov approximation as the data model turns out to be fast because of Fourier transforming measured data with respect to both time and space. This enables us to easily low-pass filter the data prior to reconstruction which reduces the amount of data entering the reconstruction considerably as well as stabilizing the whole computational procedure. In this way computational effort was reduced by more than a factor of 3.

From time-domain paraxial scanning optical mammograms of a patient carrying mastopathic disease, changes of absorption and diffusion coefficients from their background values were reconstructed in this way taking only one harmonic frequency and the nine lowest spatial Fourier components into account. Two approaches were followed to assess the reliability of the reconstructed absorption and reduced scattering coefficients. On one hand corresponding phantom experiments were carried out using paraxial scanning, measuring distributions of times of flight of photons through a scattering phantom simulating a compressed breast, containing two spherical inhomogeneities representing pure absorbers. Subsequently the optical properties of the phantom were reconstructed by our fast inverse Fourier space method from logarithmic data normalized to the (global) average over all measured data (approximate normalization) or data measured for the homogeneous phantom (proper normalization). Reconstructed optical properties were compared with the known phantom optical properties. We conclude from our phantom experiments that on one hand cross-talk between reconstructed absorption and reduced scattering coefficients occurs, on the other hand considerable blurring of the absorption coefficient along the compression direction, compromising (longitudinal) spatial resolution, because of the limited angular data provided by paraxial scanning. In addition, (approximate) normalization of the data degrades longitudinal resolution compared to proper normalization. To improve longitudinal resolution recording data at larger projection angles, i.e. larger lateral source–detector offsets is required. However, scanning the source and detector optical fibres does not lend itself easily for recording data *in vivo* at large projection angles. Probably stationary source–detector arrangements offer advantages in this respect.

On the other hand, for validation we compared reconstructed *in vivo* absorption and reduced scattering coefficients with (projection) mammograms, directly derived from experimental data. For this purpose mammograms were generated by time-window analysis of the measured temporal point spread functions. Additionally average absorption and reduced scattering coefficients were derived from measured distributions of times of flight within a simple homogeneous model and used to generate absorption and scattering projection mammograms. Projection mammograms based on time-window analysis or average absorption coefficients displayed several inhomogeneities including the mastopathy that could also be identified in the reconstructed absorption images. However, projection

mammograms do not provide any resolution along the compression direction, and hence mammograms displaying absorption and reduced scattering coefficients reconstructed from paraxial scanning data yield additional information capable to improve the diagnostic impact of optical mammography. Yet the additional information provided by reconstructed absorption and scattering mammograms is limited to some extent by blurring and cross-talk, for example, and further investigations are required to improve longitudinal resolution and to reduce artefacts. To this end open questions need to be answered as to, for example, the optimal number of source–detector offsets in *in vivo* measurements, optimal normalization schemes or even more suitable regularization strategies for this specific inverse problem.

Acknowledgments

This work was supported in part by the European Commission, contract QL G1-CT-2000-00690.

References

- Arridge S R 1999 Optical tomography in medical imaging *Inverse Problems* **15** R41–93
- Arridge S R, Schweiger M, Hiraoka M and Delpy D T 1993 A finite element approach for modelling photon transport in tissue *Med. Phys.* **20** 299–309
- Cerussi A E, Jakubowski D, Shah N, Bevilacqua F, Lanning R, Berger A J, Hsiang D, Butler J, Holcombe R F and Tromberg B J 2002 Spectroscopy enhances the information content of optical mammography *J. Biomed. Opt.* **7** 60–71
- Colak S B, van der Mark M B, 't Hooft G W, Hoogenraad J H, van der Linden E S and Kuijpers F A 1999 Clinical optical tomography and NIR spectroscopy for breast cancer detection *IEEE J. Sel. Top. Quantum Electron.* **5** 1143–58
- Culver J P, Choe R, Holboke M J, Zubkov L, Durduran T, Slemp A, Ntziachristos V, Chance B and Yodh A G 2003 Three-dimensional diffuse optical tomography in the parallel plane transmission geometry: evaluation of a hybrid frequency domain-continuous wave clinical system for breast imaging *Med. Phys.* **30** 235–47
- Dehghani H, Pogue B W, Poplack S P and Paulsen K D 2003 Multiwavelength three-dimensional near-infrared tomography of the breast: initial simulation, phantom, and clinical results *Appl. Opt.* **42** 135–45
- Franceschini M A, Moesta K T, Fantini S, Gaida G, Gratton E, Jess H, Mantulin W W, Seeber M, Schlag P M and Kaschke M 1997 Frequency-domain techniques enhance optical mammography: initial clinical results *Proc. Natl. Acad. Sci. USA* **94** 6468–73
- Gandjbakhche A H, Chernomordik V, Hebden J C and Nossal R 1998 Time-dependent contrast functions for quantitative imaging in time-resolved transillumination experiments *Appl. Opt.* **37** 1973–81
- Götz L, Heywang-Köbrunner S H, Schütz O and Siebold H 1998 Optical mammography on preoperative patients (Optische Mammographie an präoperativen Patientinnen) *Akt. Radiol.* **8** 31–3
- Grosenick D, Moesta K T, Wabnitz H, Mucke J, Stroszczynski C, Macdonald R, Schlag P M and Rinneberg H 2003 Time-domain optical mammography: Initial clinical results on detection and characterization of breast tumors *Appl. Opt.* **42** 3170–86
- Grosenick D, Wabnitz H, Moesta K T, Mucke J, Schlag P M and Rinneberg H 2005 Time-domain scanning optical mammography: II. Optical properties and tissue parameters of 87 carcinomas *Phys. Med. Biol.* **50** 2451–68
- Grosenick D, Wabnitz H, Rinneberg H, Moesta K T and Schlag P 1999 Development of a time-domain optical mammograph and first *in vivo* applications *Appl. Opt.* **38** 2927–43
- Kak A C and Slaney M 1988 *Principles of Computerized Tomographic Imaging* (New York: IEEE Press) chapter 7
- Klose A D and Hielscher A H 1999 Iterative reconstruction scheme for optical tomography based on the equation of radiative transfer *Med. Phys.* **26** 1698–707
- Li X D, Durduran T, Yodh A G, Chance B and Pattanayak D N 1997 Diffraction tomography for biochemical imaging with diffuse photon density waves *Opt. Lett.* **22** 573–5
- Li X D, Pattanayak D N, Durduran T, Culver J P, Chance B and Yodh A G 2000 Near-field diffraction tomography with diffuse photon density waves *Phys. Rev. E* **61** 4295–309
- Markel V A and Schotland J C 2001 Inverse problem in optical diffusion tomography. I. Fourier–Laplace inversion formulas *J. Opt. Soc. Am. A* **18** 1336–47

- Markel V A and Schotland J C 2002a Inverse problem in optical diffusion tomography. II. Role of boundary conditions *J. Opt. Soc. Am. A* **19** 558–66
- Markel V A and Schotland J C 2002b Scanning paraxial optical tomography *Opt. Lett.* **27** 1123–5
- Markel V A and Schotland J C 2002c Effects of sampling and limited data in optical tomography *Appl. Phys. Lett.* **81** 1180–2
- Markel V A and Schotland J C 2004 Symmetries, inversion formulas, and image reconstruction for optical tomography *Phys. Rev. E* **70** 056616-1–056616-19
- O’Leary M A 1996 Imaging with diffuse photon density waves *PhD thesis* University of Pennsylvania
- O’Leary M A, Boas D A, Chance B and Yodh A G 1995 Experimental images of heterogeneous turbid media by frequency-domain diffusing-photon tomography *Opt. Lett.* **20** 426–8
- Paulsen K D and Jiang H 1995 Spatially-varying optical property reconstruction using a finite element diffusion equation approximation *Med. Phys.* **22** 691–701
- Pifferi A, Taroni P, Torricelli A, Messina F, Cubeddu R and Danesini G 2003 Four-wavelength time-resolved optical mammography in the 680–980-nm range *Opt. Lett.* **28** 1138–40
- Ripoll J, Ntziachristos V and Nieto-Vesperinas M 2001 The Kirchhoff approximation for diffusive waves *Phys. Rev. E* **64** 1–8
- Schweiger M, Arridge S R and Delpy D T 1993 Application of the finite-element method for the forward and inverse models in optical tomography *J. Math. Imaging Vision* **3** 263–83
- Schweiger M, Arridge S R, Hiroaka M and Delpy D T 1995 Application of the finite-element method for the forward and inverse models in optical tomography *Med. Phys.* **22** 1779–92
- Walker A, Fantini S and Gratton E 1997 Image reconstruction by backprojection from frequency-domain optical measurements in highly scattering media *Appl. Opt.* **36** 170–9
- Yates T, Hebden J C, Gibson A, Everdell N, Arridge S R and Douek M 2005 Optical tomography of the breast using a multi-channel time-resolved imager *Phys. Med. Biol.* **50** 2503–17